American Mineralogist, Volume 108, pages 1692–1707, 2023

# Grain-scale zircon Hf isotope heterogeneity inherited from sediment-metasomatized mantle: Geochemical and Nd-Hf-Pb-O isotopic constraints on Early Cretaceous intrusions in central Lhasa Terrane, Tibetan Plateau

Ming-Jian Li[1,2], Yun-Chuan Zeng[1,*], Massimo Tiepolo[2], Federico Farina[2], Ji-Feng Xu[1], Feng Huang[1], Xi-Jun Liu[3], Qin Chen[4], and Yuan Ma[5]

[1]State Key Laboratory of Geological Processes and Mineral Resources, School of Earth Science and Resources, China University of Geosciences, Beijing 100083, China
[2]Dipartimento di Scienze della Terra "A. Desio", Università degli Studi di Milano, Via Botticelli 23, Milano 20133, Italy
[3]Guangxi Key Laboratory of Hidden Metallic Ore Deposits Exploration, College of Earth Sciences, Guilin University of Technology, Guilin 541004, China
[4]The Second Geological Exploration Institute of China Metallurgical Geology Bureau, Fuzhou 350108, China
[5]China Railway Design Corporation, Tianjin 300142, China

## Abstract

Clarifying the mechanism of recycling of pre-existing continental crustal materials into the source of mantle-derived magma is a challenging effort that can be of great value to improving our understanding of mantle processes and continental crust growth. This study presents an integrated investigation of whole-rock and mineral geochemical and Nd-Hf-O-Pb isotopic data for dolerites and diorites intruded in the central Lhasa Terrane of Tibetan Plateau at ca. 120 Ma (zircon U-Pb ages). These intrusions have similar distributions of trace elements that are characterized by depletion in Nb-Ta relative to Th, Ba, and U, and moderately negative whole-rock $\varepsilon_{Nd}(t)$ (–5.0 to –1.7) values. Magmatic zircon shows dramatically variable $\varepsilon_{Hf}(t)$ values (from –5.0 to +13.7 in the same rock, including up to 12 epsilon unit variability in single grains). On the other hand, the zircon $\delta^{18}O$ values are relatively uniform (+6.0‰ to +7.7‰). The constant $^{208}Pb/^{206}Pb$ values of clinopyroxene crystallized at ca. 500–900 MPa suggest no contamination with lower continental crust. The lack of covariation between Hf and O isotopes from the same grains, and the lack of relationship between Hf isotopes and trace elements (e.g., Hf, Th/U, and Yb/Gd) in the magmatic zircons, together with the absence of ancient zircon xenocrysts, imply limited upper crustal contamination. In combination with high-whole-rock Th/La (>0.29) ratios, we interpret the zircon Hf isotope heterogeneity as inherited from a depleted asthenospheric mantle with the addition of 1–4% Hf from isotopically heterogeneous sediments. Our study therefore emphasizes the need for caution when using complex Hf isotopic zonation in zircon as an argument for intracrustal hybridization of two end-member magmas derived from distinct reservoirs. In addition, the high-Zr/Y ratios and no negative Zr-Hf anomalies of the Aruo intrusions imply a high surface temperature of the down going slab that was able to fully dissolve zircons in the subducted sediments. This requires a special geodynamic condition that was most likely related to the steepening of flatly subducted Neo-Tethyan lithosphere at ca. 120 Ma according to a synthesis of regional tectonic-magmatic-sedimentary records.

**Keywords:** Zircon Hf heterogeneity, sedimentary recycling, mantle metasomatism, magma mixing, Lhasa Terrane

## Introduction

Recycling of pre-existing continental crustal materials in magmatic arcs is a fundamental process controlling the chemistry and evolution of the continental crust. The involvement of a crustal component in arc-related magmas has been widely recognized and is typically manifested by the enriched radiogenic (e.g., Sr-Nd-Hf) isotope composition. This can be achieved in two profoundly different ways, either in the mantle through the addition of subducted material (mostly sediments), or in the crust by assimilation and contamination of mantle-derived precursors (e.g., Hawkesworth and Vollmer 1979; Gasparon et al. 1994). Distinguishing the two opposing mechanisms is not easy unless unequivocal evidence, for example sediment-derived magmas intruding the peridotite mantle wedge, is preserved (e.g., Zeng et al. 2016; Spencer et al. 2017), but is crucial to determining the rates and volumes of continental growth and recycling.

Zircon is an ideal mineral to trace source complexity and evolution of the parent magma, as it is chemically stable and has the potential to provide information on crystallization age (U-Pb), radiogenic (Hf), and stable (O) isotopes, as well as on melt compositions (Valley et al. 2005; Kemp et al. 2007; Grimes et al. 2015). Studies based on combined U-Pb, Hf, and O isotopes measured within single zircon grains have significantly advanced our capacity to understand the role of mantle and sediment (or mature continent crust) components in the petrogenesis of granitoid, as well as to enhance our insight into the timing of continental crust growth (e.g., Kemp et al. 2007). Substantial variation of zircon $\varepsilon_{Hf}(t)$ values has been recognized in granitoid worldwide and is commonly interpreted as evidence of mixing of magma derived from isotopically different reservoirs (Kemp

* E-mail: zengyc@cugb.edu.cn. Orcid 0000-0002-9701-9693

0003-004X/23/0009–1692$05.00/DOI: https://doi.org/10.2138/am-2022-8508

et al. 2007; Farina et al. 2018), non-equilibrium melting of individual crustal sources (Tang et al. 2014) or due to local processes involving zircon dissolution and recrystallization (Villaros et al. 2012; Farina et al. 2014; Finch et al. 2021). However, subducted sediments may also play a significant role in the Hf budget of arc magmas, as exemplified by the Banda arc where the mafic rocks underwent no or very limited crust contamination but present substantial changes in Hf isotopes ($\varepsilon_{Hf}$ = –3.8 to +12.5) with only little variation in $\delta^{18}O$ of +5.8‰ to +7.5‰ (Nebel et al. 2011). This phenomenon indicates that zircon Hf isotope heterogeneity in granitoids may occur in mafic magmas that are free from any kind of assimilation. However, in comparison with granitoids, large Hf isotopes variations at grain-scale are rather rare in zircon from mafic rocks, probably due to higher crystallization temperature and/or less abundance of zircons in mafic magma system.

In this paper, we present zircon U-Pb, Lu-Hf, and O isotopic, whole-rock geochemical and Sr-Nd isotopic, and in situ clinopyroxene elemental and Pb isotopic data, for some newly identified Early Cretaceous dolerites and diorites in the Aruo area of central Lhasa Terrane, Tibetan Plateau. The combined data sets lead us to contend that dramatic zircon Hf isotope heterogeneities are not caused by intracrustal mixing of crust- and mantle-derived magma. We argue instead that the isotopic variability is inherited from a deleted asthenospheric mantle metasomatized by 1–4% sediment with heterogeneous Hf isotopes.

## Geological background and sample descriptions

The Tibetan Plateau consists of four E-W-trending tectonic units, which from north to south are the Songpan-Ganzi, Qiangtang, Lhasa, and Himalaya terranes separated by three main suture zones (Yin and Harrison 2000). As the leading edge of the India-Asia collision, the Lhasa Terrane is sandwiched between the Bangong-Nujiang suture zone (BNSZ) and the Indus-Yarlung Zangbo suture zone (IYZSZ) (Fig. 1a). The BNSZ represents the remnants of the Meso-Tethys Ocean, which was proposed to have closed in the Late Jurassic or the Early Cretaceous (Zeng et al. 2021a). The Meso-Tethys Ocean slab has subducted northwards beneath the Qiangtang Terrane since Early Jurassic (Li et al. 2014, 2020), but it remains controversial whether this paleo-ocean slab has ever subducted toward south beneath the Lhasa Terrane (e.g., Zeng et al. 2018; Li et al. 2018). The IYZSZ represents the remnants of the Neo-Tethyan lithosphere that started to subduct beneath the Lhasa Terrane at Middle Triassic and closed at Early Paleogene following the suturing of Indian and Asian continents (Kang et al. 2014; Kapp and DeCelles 2019).

Based mainly on plentiful zircon $\varepsilon_{Hf}$ data from intermediate-felsic igneous rocks and sediment cover, the Lhasa Terrane can be divided into northern, central, and southern parts, separated by the Shiquan River-Nam Tso Mélange Zone and the Luobadui-Milashan Fault, respectively (Fig. 1; Zhu et al. 2011a). The northern Lhasa Terrane is covered by Middle Triassic-Cretaceous sedimentary rocks and contains widespread Early Cretaceous magmatic rocks which predominantly have positive zircon $\varepsilon_{Hf}$ values. The magmatic rocks exposed in the central Lhasa terrane are dominantly Early Cretaceous granitoid and volcanic rocks. The zircon $\varepsilon_{Hf}$ values of these rocks are rather negative, which, in combination with the Cambrian-Paleozoic sediment cover, likely suggests the presence of ancient basement materials. The southern Lhasa terrane is mainly composed of Jurassic-Paleogene Gangdese batholith and associated volcanic successions (Ji et al. 2009; Kang et al. 2014). The overall positive zircon $\varepsilon_{Hf}$ values of the Mesozoic magmatic rocks of this subterrane indicate a juvenile nature of the continental crust, although Precambrian basement has been locally identified in eastern and western parts (Hou et al. 2015).

Samples in the present study were collected from the northeast bank of the Kering Lake, ~70 km northwest of Xainza Town (Fig. 1), which tectonically belongs to the central Lhasa Terrane. In addition to Quaternary deposits, the strata exposed in the study area are mainly composed of Devonian Chaguolama Formation limestone; Permian Xiala Formation limestone, Angjie Formation shale, mudstone and siltstone; and Lower Cretaceous Duoni Formation sandstone, siltstone and mudstone. The dolerites and diorites occur as intrusions with irregular map patterns, with diameters hundreds of meters, which intruded the siltstones of the Lower Permian Angjie Formation (Fig. 1b) in the Early Cretaceous, based on previous K-Ar dating (134 Ma; Wang et al. 2002). In addition, some Early Cretaceous basalts-basaltic andesites are exposed to the south of the Aruo intrusions (Fig. 1b; Kang 2009).

The Aruo dolerites and diorite are medium-fine-grained and are mainly composed of euhedral plagioclase, subhedral to euhedral clinopyroxene and amphibole with accessory minerals such as titanite, zircon, ilmenite, and apatite. In addition, some pyroxene and plagioclase grains have been converted to epidote by post-emplacement alteration (Fig. 2). It is noteworthy that some of the euhedral plagioclase grains are wrapped by clinopyroxene and amphibole (Figs. 2b–2c) suggesting that plagioclase crystallized before clinopyroxenes and amphiboles.

## Analytical methods

### Zircon U-Pb, O, and Lu-Hf isotope analyses

Zircons were separated by standard density and magnetic separation techniques and individually selected by hand-picking under a binocular microscope. Zircon oxygen isotope analyses were carried out before U-Pb and Lu-Hf isotope determinations. Zircon oxygen isotopes were measured using the SHRIMP IIe-MC equipped with a Cs ion source at the Beijing SHRIMP Center. During the analysis, a 3 nA beam of $Cs^+$ was focused into a spot 20 μm elliptical on the target surface. The detailed analytical procedures were similar to those described by Ickert et al. (2008). The measured oxygen isotopic data were corrected for instrumental mass fractionation using the Qinghu zircon ($\delta^{18}O_{VSMOW}$ = +5.3‰) as the external standard (Li et al. 2013). Eleven measurements of the internal standard PengLai zircon grains yield a weighted mean of $\delta^{18}O$ = +5.30 ± 0.19‰, which is identical within errors to the reported value of +5.31 ± 0.10‰ (Li et al. 2010). Measured $^{18}O/^{16}O$ is normalized to VSMOW, and then corrected for the instrumental mass fractionation factor (IMF) as follows: $(\delta^{18}O)_M = [(^{18}O/^{16}O)_M/0.0020052 - 1] \times 1000$; $IMF = (\delta^{18}O)_{M(standard)} - (\delta^{18}O)_{VSMOW}$; $\delta^{18}O_{sample} = (\delta^{18}O)_M + IMF$.

Zircon U-Pb isotopic analyses were conducted in five analytical sessions using laser ablation-inductively coupled plasma-mass spectrometry (LA-ICP-MS) at the Guilin University of Technology (GUT). Cathodoluminescence images were used to select the appropriate zircon grains for analysis. Laser sampling was performed using a GeoLasHD LA system. An Agilent 7900 ICP-MS instrument was used to acquire ion-signal intensities. A detailed description of the laboratory and sample preparation methods, following the guidelines in http://www.plasmage.org/recommendations and recommended in Horstwood et al. (2016) are available as metadata (Online Materials[1] Table S1). Prior to sample analysis, an additional nitrogen gas flow (4 mL/min) was used to improve the instrumental sensitivity. Helium and Ar were the carrier and the makeup gas, respectively, and were mixed via a *T*-connector before entering the ICP. Following about 20 s period of background analysis, samples were spot ablated for 60 s at a 6 Hz repetition rate with a spot size of 32 μm beam and laser energy of 10 J/cm$^2$ at the sample surface. Plesovice zircon ($^{206}Pb/^{238}U$ age = 337 Ma; Sláma et al. 2008) and NIST 610 were

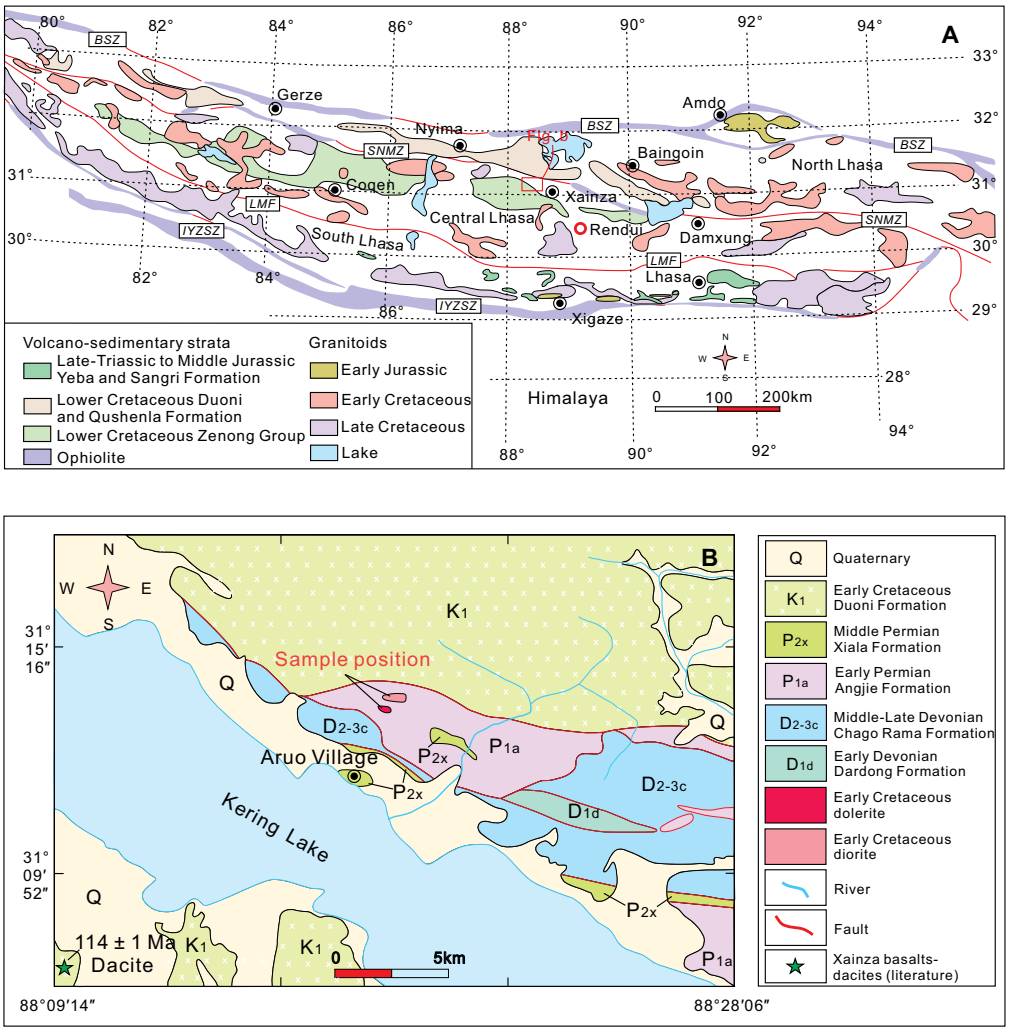


**FIGURE 1.** (**a**) Simplified tectonic map of the Tibetan Plateau showing the distribution of Mesozoic magmatic rocks of the Lhasa Terrane (after Zeng et al. 2020). (**b**) Geological map of the Aruo region, central Lhasa Terrane. IYZSZ = Indus-Yarlung Zangbo Suture Zone; BSZ = Bangong Suture Zone; SNMZ = Shiquanhe-NamuTso ophiolite mélange zone; LMF = Lobuodui-Milashan Fault. The zircon age (zircon U-Pb) of the Xainza basalts-dacites is from Kang (2009).

analyzed as U-Pb and trace element external standards, respectively. GJ-1 standard zircon was measured as unknown samples to the quality of monitor trace elements. During the course of this study, the analyzed GJ-1 standard zircon grains yielded a weighted $^{206}Pb/^{238}U$ age of 605 ± 1 Ma (1σ, MSWD = 0.3, n = 40; Online Materials[1] Table S2), which is consistent with the recommended U-Pb age in allowed precision ($^{206}Pb/^{238}U$ age = 608.5 ± 0.4 Ma; Jackson et al. 2004). In addition, the trace element concentrations of GJ-1 standard zircon were also consistent with the reference values (Online Materials[1] Table S3).

The Lu–Hf isotopic compositions of dated zircons were determined using an MC–ICP–MS coupled with the laser ablation system at GUT. Analyses were conducted using a beam diameter of 44 μm and a laser pulse frequency of 10 Hz. The GJ-1 zircon was used as an external standard to monitor data quality. The ratios of $^{176}Lu/^{175}Lu = 0.02655$, $^{172}Yb/^{176}Yb = 0.5887$, $\beta Yb = 0.8725 \times \beta Hf$ ($\beta Hf$ and $\beta Yb$ refer to the mass bias of Hf and Yb, respectively) obtained were used in the isobaric interference correction, consistent with the reference value (Wu et al. 2006). The stable $^{178}Hf/^{177}Hf$ and $^{180}Hf/^{177}Hf$ ratios of GJ-1 zircon grains analyzed in this study were 1.46715 ± 0.00023 and 1.88689 ± 0.00024 (2σ, n = 48), respectively, which are within 200 ppm of known values based upon atomic masses and abundances as recommended by Spencer et al. (2020). The $^{176}Hf/^{177}Hf$ ratios of GJ-1 zircon grains range from 0.281970 ± 16 to 0.282048 ± 20 with a mean value of 0.282009 ± 0.000016 (2σ; n = 48), consistent with the reference value (0.282015 ± 0.000019, 2σ; Elhlou et al. 2006) within allowed analytical errors.

## Whole-rock major and trace elements analyses

Major and trace element analyses were conducted using an XRF-1500 X-ray fluorescence analyzer and a double focusing high-resolution inductively coupled plasma-mass spectrometer (ICP-MS) at the Institute of Geology and Geophysics, Chinese Academy of Sciences. The loss on ignition (LOI) values were measured first. About 2.0 g powdered samples were baked in the muffle furnace for more than 2 h at 915 °C. Then about 0.6 g baked samples were fluxed with $Li_2B_4O_7$ (6 g) at ~1200 °C to make homogeneous glass disks for major elements determination. During analysis, the USGS standard reference materials (GSR-1, GSR-2, and GSR-3) were used to monitor the data quality. The analytical precision was better than 5%.

For trace elements analysis, 40 mg sample powders were dissolved in polytetrafluoroethylene bakers using a hybrid acid (1 mL 22 M HF, 0.5 mL 8 M $HNO_3$) at 120 °C. Then the solutions were dried and the residues were dissolved using the hybrid acid (1.5 mL 22 M HF, 0.5 mL 8 M $HNO_3$) and placed into high-pressure vessels at 200 °C for 5 days. After that, the sample solutions were dried again and dissolved with 2.0 mL 8 M $HNO_3$ in the vessels at 150 °C for 24 h. After repeating the previous steps, solutions were transferred into PE bottles with 50 g 1% $HNO_3$ containing 10 ppt In. During the procedure, the USGS standard reference materials (GSR-1, GSR-2, and GSR-3) and two blank samples were taken as the external calibration standards. The analytical precision was better than 10%.

## Whole-rock Sr-Nd isotope analyses

Powdered samples (~100 mg) for Sr and Nd isotopic analyses were dissolved first using a 1:3 mixture of HF and $HNO_3$ for 7 days at 120 °C in PFA beakers. The solutions were evaporated to approximatively dry at 120 °C, and the residues were dissolved in 16 M $HNO_3$ and then evaporated again. Subsequently, the residues were re-dissolved in 1 mL 16 M $HNO_3$, and insulated at 120 °C for over 4 h. The solutions were re-evaporated at 120 °C, and the residues were dissolved in 2 mL 2 M

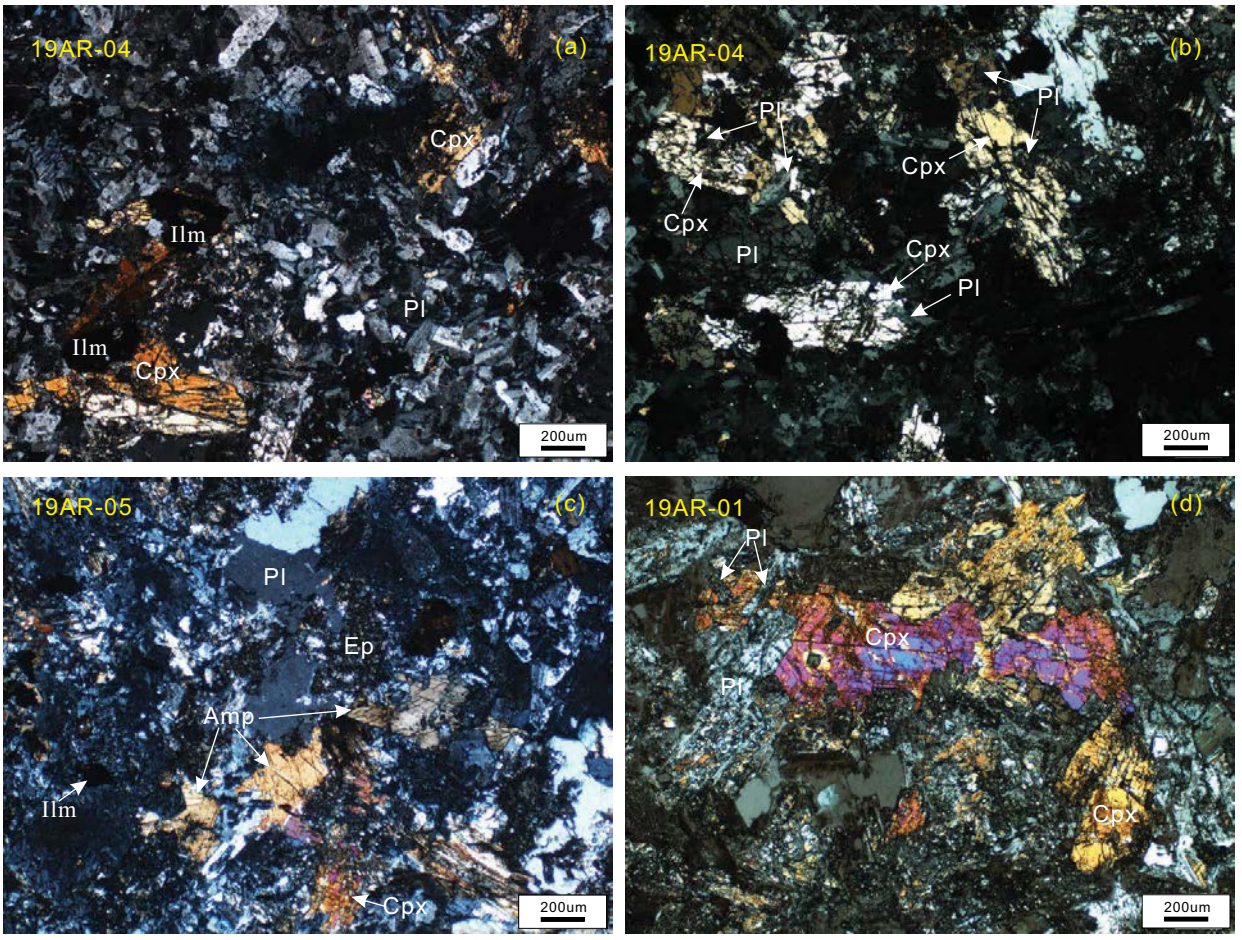


**Figure 2.** Representative photomicrographs (cross-polarized illumination) showing the mineral assemblages of the Aruo dolerites (**a**–**c**) and diorites (**d**). Pl = plagioclase; Cpx = clinopyroxene; Amp = amphibole; Ilm = ilmenite; Ep = epidote.

$HNO_3$ at 120 °C for over 2 h, which were centrifuged and prepared to separation of the target elements. Strontium and rare earth elements (REE) were separated using a cationic resin. The REE solutions was then processed through HDEHP resin to obtain purified Nd. Strontium and neodymium isotopes were measured by Neptune Plus multi-collector (MC)-ICP-MS at GUT. The Sr and Nd isotopic data were obtained on MC-ICP-MS and normalized to $^{86}Sr/^{88}Sr = 0.1194$ and $^{146}Nd/^{144}Nd = 0.7219$, respectively. $^{87}Rb/^{86}Sr$ and $^{147}Sm/^{144}Nd$ ratios were calculated from abundances of these trace elements measured by ICP-MS. The USGS standard reference materials (BHVO-2, GSR-1, and GSR-3) were used to monitor the data quality. The Sr and Nd isotopes of BHVO-2 ($^{87}Sr/^{86}Sr = 0.703542 \pm 6$, $^{143}Nd/^{144}Nd = 0.512959 \pm 5$), GSR-1 ($^{87}Sr/^{86}Sr = 0.738340 \pm 7$, $^{143}Nd/^{144}Nd = 0.512217 \pm 6$), and GSR-3 ($^{87}Sr/^{86}Sr = 0.704131 \pm 6$, $^{143}Nd/^{144}Nd = 0.512892 \pm 5$) are consistent with the reference values (Weis et al. 2006; Bao et al. 2018).

### In situ elemental and Pb isotopic compositions of minerals

Major element compositions of clinopyroxene and amphibole were determined using a JOEL JXA 8230 electron microprobe at the Shandong Analysis Center of China Metallurgical Geology Bureau. Analytical conditions for the electron microprobe were 15 kV accelerating voltage, 20 nA beam current, 10–20 s counting time and 10 μm electron beam diameter. Natural and synthetic materials were used as standards.

Major and trace elements of clinopyroxene were measured by the LA-ICP-MS at the GUT. Laser ablation was undertaken at a constant energy 10 J/cm$^2$ and at 10 Hz with a spot diameter of 46 μm. Trace element concentrations were calibrated using international standards including NIST 610, BCR-2G, BIR-1G, and BHVO-2G. Detailed analytical methods and the operating conditions for the laser ablation system are given by Liu et al. (2008).

In situ analysis of Pb isotopes in clinopyroxene used MC-ICP-MS (Thermo Scientific) equipped with a 193 nm laser ablation system (Resonetics) at the Guangzhou Institute of Geochemistry, Chinese Academy of Sciences. An X-skimmer cone and additional nitrogen gas flow (2 mL/min) were used to improve the instrumental sensitivity. Isotope signals were detected with ion counters in the static mode. During the first 28 s, the gas blank of the system was monitored. In the following 30 s, the signals of laser ablation on clinopyroxene were collected. The analytical procedures were described in detail by Zhang et al. (2014). Repeated analyses of the international basaltic glass BHVO-2G yielded mean values of $^{208}Pb/^{206}Pb = 2.054 \pm 0.004$ (2σ, n = 9) and $^{207}Pb/^{206}Pb = 0.833 \pm 0.001$ (2σ, n = 9), which are consistent with the reported values (2.048 and 0.832, respectively) (Elburg et al. 2005; Zhang et al. 2014).

## Results

Analytical results from zircon (O and Lu-Hf isotopes, U-Pb ages, and trace elements), whole rocks (Sr and Sm-Nd isotopes, major and trace elements), and clinopyroxenes (trace elements and Pb isotopes) are listed in Online Materials[1] Tables S2–S9.

### Zircon U-Pb ages and trace elements

Zircons separated from two dolerite samples (18AR-01 and 19AR-03) and one diorite sample (19AR-01) were analyzed for U-Pb isotopes and trace elements (Online Materials[1] Tables S2–S3). All zircon grains were colorless and subhedral to euhedral, have variable sizes (~50–300 μm) with length-to-width

ratios of 1:1 to 3:1, display high-Th/U ratios (1.4–2.8), and present clear oscillatory or banded zoning in cathodoluminescence images (Fig. 3).

A total of 65 zircons from sample 18AR-01 were analyzed, seven of which did not yield concordant results, probably because of Pb loss, although they have similar $^{206}Pb/^{238}U$ ages to those of the other zircons. The remaining 58 spots yielded similar concordant zircon $^{206}Pb/^{238}U$ ages varying from 125.3 ± 2 to 117.4 ± 2 Ma with a weighted mean of 119.7 ± 0.5 Ma (±1σ, MSWD = 0.43; Fig. 4a). Similarly, 107 of 115 analytical spots on zircons from sample 19AR-03 yielded concordant zircon $^{206}Pb/^{238}U$ ages varying from 124.7 ± 1 to 117.0 ± 3 Ma with a weighted mean of 119.9 ± 0.3 Ma (±1σ, MSWD = 0.75; Fig. 4b). Nineteen of 26 analytical spots on zircon grains from sample 19AR-01 yielded concordant zircon $^{206}Pb/^{238}U$ ages varying from 120.4 ± 2 to 117.0 ± 1 Ma with a weighted mean age of 118.6 ± 0.7 Ma (±1σ, MSWD = 0.72; Fig. 4c). Our new zircon geochronological data imply that the Aruo diorites and dolerites were coevally formed at ca.120 Ma instead of 134 Ma as suggested previously by K-Ar dating (Wang et al. 2002).

The chondrite normalized rare earth element (REE) patterns of the analyzed zircon grains are similar and are characterized by positive Ce and negative Eu anomalies, strong depletions in light (L)REE relative to heavy (H)REE (Fig. 4d).

### Zircon Lu-Hf and O isotopes

The $(^{176}Hf/^{177}Hf)_i$ of zircons from dolerites (a total of 291 analyses on zircon grains of sample 18AR-01 and 19AR-03) exhibit a wide range of 0.282557 to 0.283084 with corresponding $\varepsilon_{Hf}(t)$ values of –5.0 to +13.7 and $T_{DM\text{-}Hf}$ ages (Hf-depleted mantle model ages; Griffin et al. 2000) of 258–1224 Ma (Fig. 5; Online Materials[1] Table S4). The $\varepsilon_{Hf}(t)$ heterogeneity is also observed in

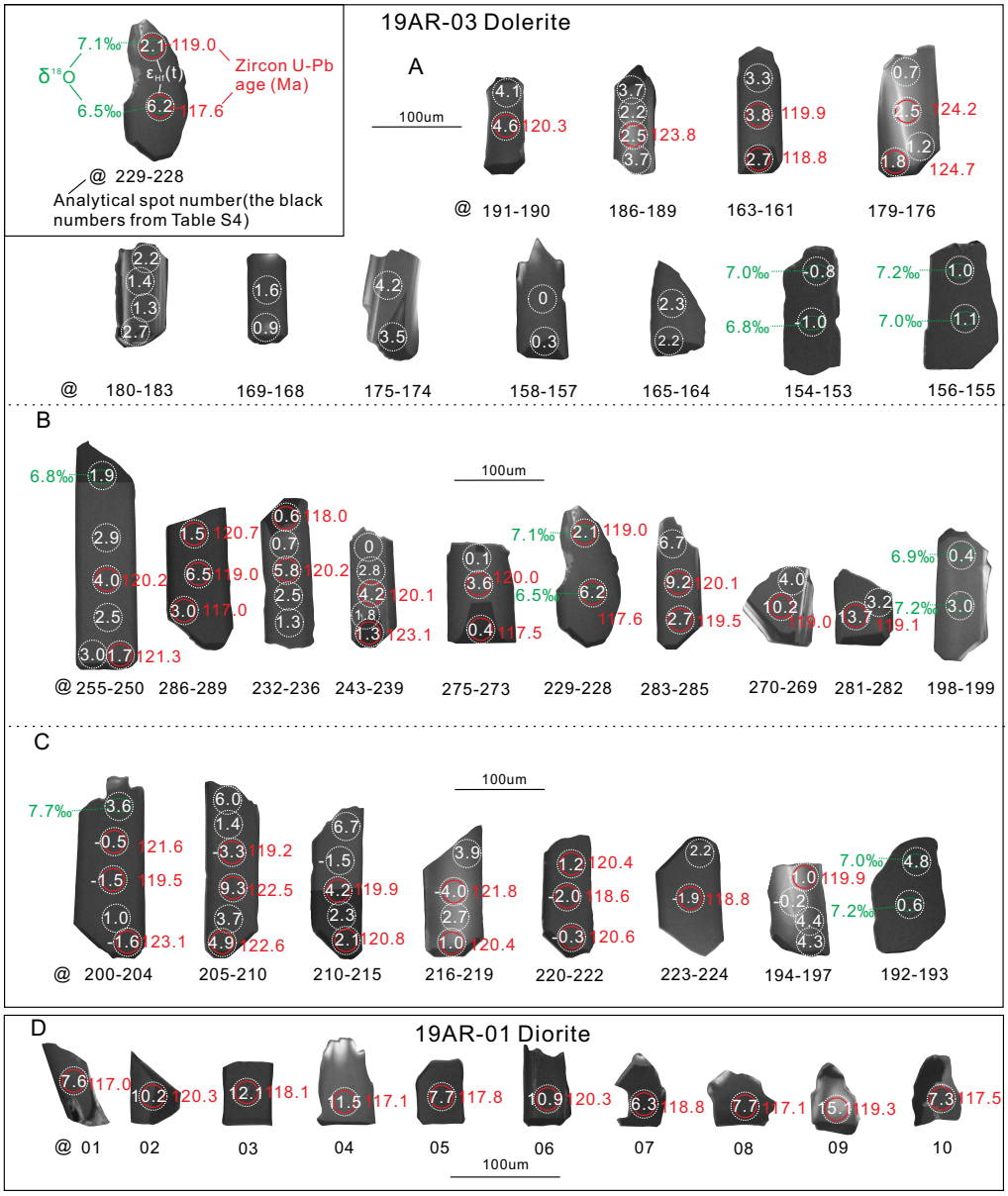


**FIGURE 3.** Representative cathodoluminescence (CL) images showing the morphology, $^{206}Pb/^{238}U$ age (Ma), and Hf-O isotopes of the zircon crystals in the Aruo dolerites and diorites.

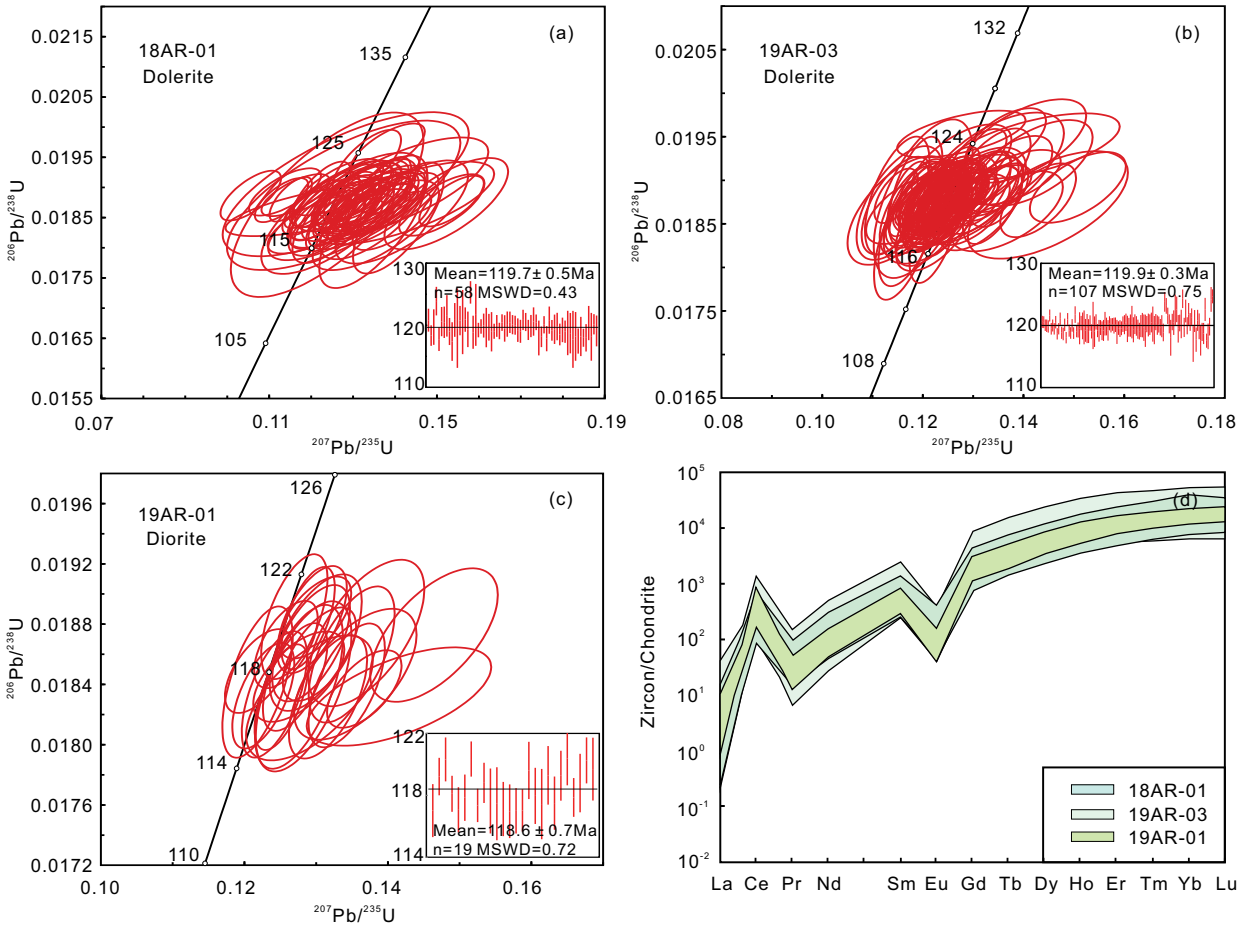


**Figure 4.** (**a**–**c**) Zircon U-Pb concordia diagrams of the Aruo dolerites and diorites, (**d**) chondrite-normalized zircon rare earth element patterns for the Aruo dolerites and diorites [normalizing values are from Sun and McDonough (1989)].

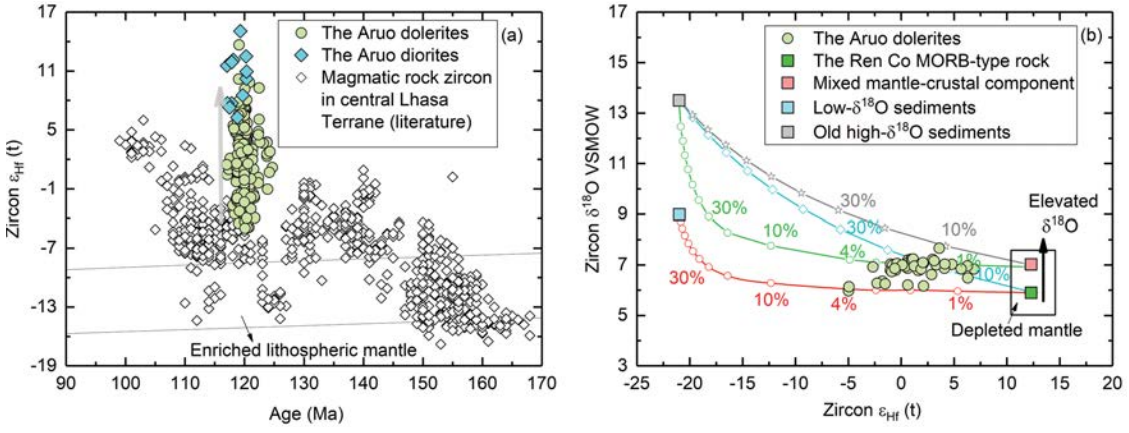


**Figure 5.** Plots of (**a**) zircon age vs. $\varepsilon_{Hf}(t)$ and (**b**) zircon $\varepsilon_{Hf}(t)$ vs. $\delta^{18}O$. In **b**, the curves are binary mixtures of putative mantle and crustal end-members (upper continental crust). The basalt was represented by the Jurassic MORB-type rock (15T160) in the Ren Co region (Tang et al. 2020), and the upper crust was represented by the Baingoin S-type granite (16BG50–5; Hu et al. 2019). Mixing with upper continental crust with different $\delta^{18}O$ values is modeled given the substantially varied zircon $\delta^{18}O$ values of the Bangoin S-type granites (Hu et al. 2019), and a mantle end-member with moderately elevated $\delta^{18}O$ value is assumed and modeled because the zircons in the Aruo intrusions with asthenosphere-like $\varepsilon_{Hf}(t)$ values also display $\delta^{18}O$ value higher than those in equilibrium with mantle-derived magmas (e.g., Roberts et al. 2013).

some individual grains with up to 12 epsilon units in the same individual grain (Figs. 3 and 5). Besides, the $\varepsilon_{Hf}(t)$ values vary irregularly. For example, as shown in Figure 3, low-$\varepsilon_{Hf}(t)$ core with high-$\varepsilon_{Hf}(t)$ rim, high-$\varepsilon_{Hf}(t)$ rim with low-$\varepsilon_{Hf}(t)$ core, are both developed. In addition, repeatedly varied $\varepsilon_{Hf}(t)$ values are observed in the same individual grain (Fig. 3c). Thirteen zircon grains from diorite sample (19AR-01) also exhibit heterogeneous $(^{176}Hf/^{177}Hf)_i$ values of 0.282908 to 0.283141, with corresponding $\varepsilon_{Hf}(t)$ values of +6.3 to +15.1 and $T_{DM\text{-}Hf}$ ages of 190 to 768 Ma.

The zircons of dolerite (sample 19AR-03) have restricted variability in oxygen isotopes with $\delta^{18}O$ values of +6.0‰ to +7.2‰ (Fig. 3; Online Materials[1] Table S4) and a mean value of +6.8‰ ± 0.21‰ (±2σ; n = 42), which are slightly higher than those (+5.3 ± 0.6‰; 2σ) of igneous zircons in equilibrium with mantle-derived magmas (Valley 2003).

## Whole-rock major and trace elements

The petrographic observations (Fig. 2) and moderate LOI values (2.3–3.9 wt%) suggest that the investigated rocks were altered after emplacement. However, based on the following evidences, we contend post-emplacement alteration played a negligible role in modifying the whole-rock chemical makeup. There is no correlation between LOI and fluid-mobile major elements (e.g., $K_2O$ and $Na_2O$; not shown). Instead, the two elements are in good correlation with $TiO_2$ and $Al_2O_3$ (Online Materials[1] Fig. S1) that are relatively immobile during alteration (Dilek and Furnes 2011; Pearce 2014). In terms of trace elements, all samples display coherent chondrite-normalized REE and primitive mantle-normalized multi-element pattern (with the notable exception of Sr), suggesting that these elements were relatively immobile during metamorphism. We further test the mobility of target elements by their relationships with the most fluid-immobile elements, i.e., Nb (e.g., Kurtz et al. 2000; Hastie et al. 2007). For example, the good correlations between Nb and elements such as Y, La, Eu, Ba, and Ce, this suggests that these elements survived alteration, whereas Sr underwent significant change.

Sixteen representative Aruo intrusions were analyzed for whole-rock major and trace elements (Online Materials[1] Table S5). In the following descriptions and diagrams, the contents of all major elements were recalculated on a normalized anhydrous basis. Consistent with the petrography, the majority of the samples plot in the gabbro, gabbroic diorite and diorite fields on the $SiO_2$-$Na_2O$+$K_2O$ diagram (Fig. 6a). With increasing $SiO_2$ content, the major oxides show roughly negative (e.g., MgO, $Fe_2O_3^T$, $TiO_2$, and CaO) or positive ($Al_2O_3$, $K_2O$) relationship (Fig. 7). On the $SiO_2$ vs. FeOt/MgO plot, the Aruo intrusions show an evolutionary trend from low-K tholeiitic to calk-alkaline (Fig. 6b).

All samples show low contents of compatible elements with (Ni = 2.26–21.9 ppm, Cr = 8.22–76.2 ppm). The primitive mantle-normalized trace-element distributions exhibit enrichment in large ion lithophile elements (LILE; e.g., Rb, U), depletion in high field strength elements (e. g., Nb, Ta), and no negative Zr and Hf anomalies (Fig. 8). The Aruo intrusions show moderate enrichment in LREE relative to HREE on the chondrite-normalized patterns [$(La/Yb)_N$ = 3.74–4.97] with negligible Eu anomalies [δEu = 0.85–1.02, $\delta Eu = Eu_N/(Sm_N \times Gd_N)^{1/2}$].

## Whole-rock Sr-Nd isotopes

Ten samples were analyzed for Sr-Nd isotopes (Online Materials[1] Table S6). The initial Sr-Nd isotopes were corrected to 120 Ma based on zircon U-Pb dating. The age-corrected $(^{87}Sr/^{86}Sr)_i$ values of the Aruo intrusions are variable (0.7064 to 0.7105), probably because the original Sr contents and isotopic signature of these rocks have been disturbed by post-emplacement alteration as suggested above. In comparison, the $(^{143}Nd/^{144}Nd)_i$ values are relatively uniform (0.512239–0.512409), corresponding to $\varepsilon_{Nd}(t)$ values of –1.5 and –4.8 and $T_{DM\text{-}Nd}$ of 1295 to 2017 Ma (Fig. 9).

## Mineral chemistry

This and our previous studies (Zeng et al. 2021a, 2021b) demonstrate that the major elements of clinopyroxene obtained by the two independent techniques (LA-ICP-MS and EPMA) are identical within analytical errors; therefore, we refer to both in the following descriptions.

The clinopyroxenes in dolerites are augitic ($Wo_{36-47}En_{37-43}Fs_{15-24}$; Fig. 10) and exhibit moderately varied CaO, MgO, and FeO contents (17.14–22.28 wt%, 12.71–15.27 wt% and 8.95–14.18 wt% respectively; Online Materials[1] Table S7). Clinopyroxenes from the diorites are similar to those in the dolerites and show strong compositional variations (CaO = 16.09–21.73 wt%, MgO = 11.50–16.95 wt%, and FeO = 6.81–16.33 wt%).

The amphiboles from one dolerite sample (19AR-05) are magnesio-hornblende and tschermakitic pargasite, and have major element contents as follows: $SiO_2$ (40.02–44.25 wt%), CaO (10.39–12.33 wt%), MgO (11.48–12.55 wt%), $TiO_2$ (2.55–3.74 wt%), FeO (14.66–16.58 wt%), and $Al_2O_3$ (9.09–10.76 wt%) and contain minor amounts of $Na_2O$ (1.95–2.72 wt%) and $K_2O$

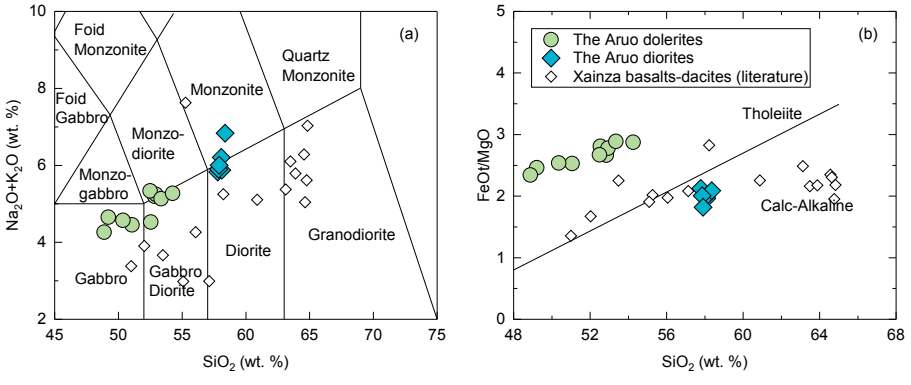


**Figure 6.** (**a**) $Na_2O + K_2O$ vs. $SiO_2$ (Middlemost 1994); (**b**) $SiO_2$ vs. $FeO_t/MgO$ diagram (after Miyashiro 1975) showing data of the Aruo intrusions. The data of the nearby Xainza basalts-dacites are plotted here and in the following geochemical diagrams for comparison because they were formed synchronously with the Aruo intrusions (Fig. 1; Kang 2009).

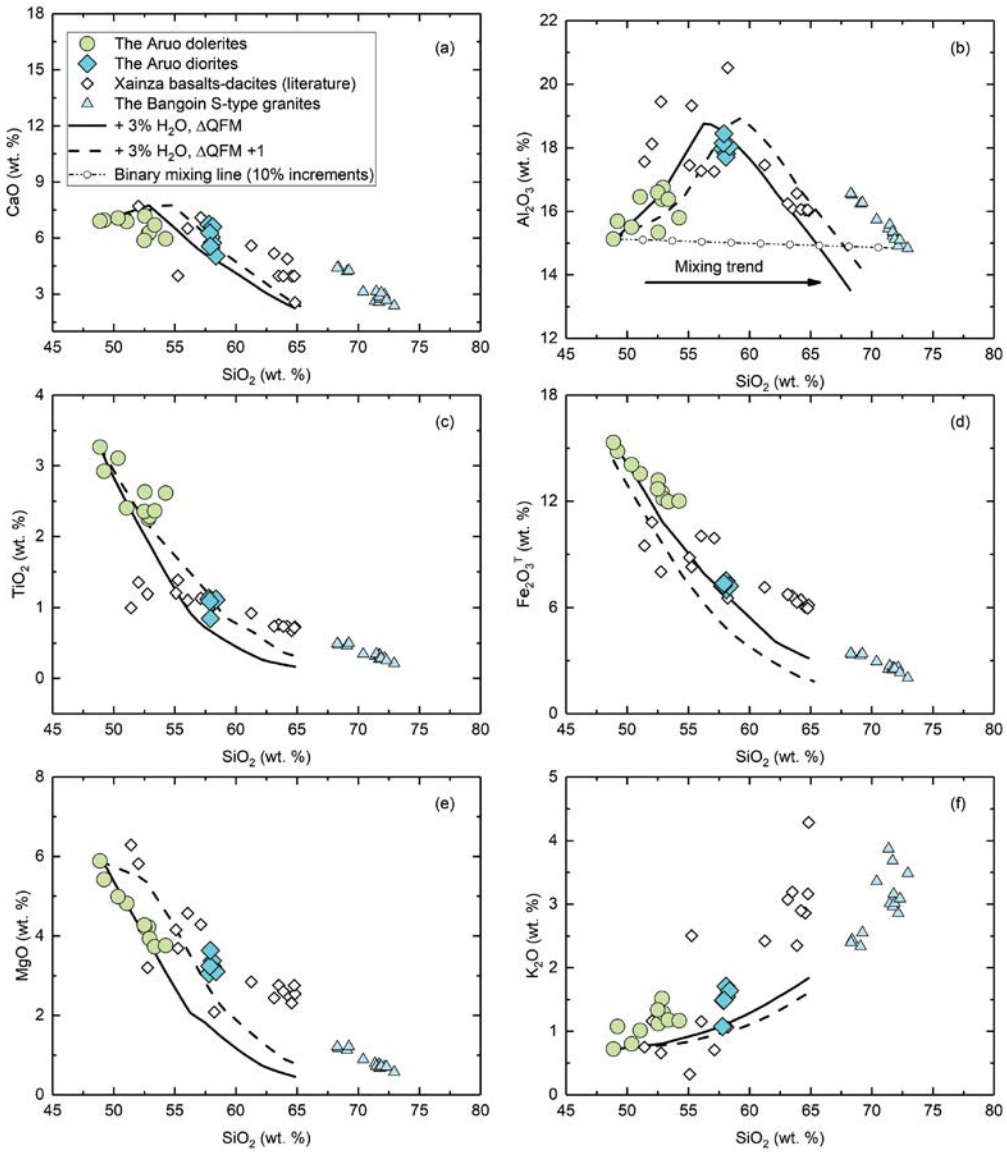


**FIGURE 7.** (**a**–**f**) Harker diagrams showing CaO, $Al_2O_3$, $TiO_2$, $Fe_2O_3^T$, MgO, and $K_2O$ vs. $SiO_2$ for the Aruo intrusions. The dashed and solid lines represent the MELTS simulated fractional crystallization trends of magma evolution (Ghiorso and Sack 1995). The model assumes that the initial magma composition is a dolerite sample 19AR-05, the water content is +3 wt%, the pressure is 200 MPa, and $f_{O_2}$ = ΔQFM ~ΔQFM+1. The data of the Xainza basalts-dacites are from Kang (2009).

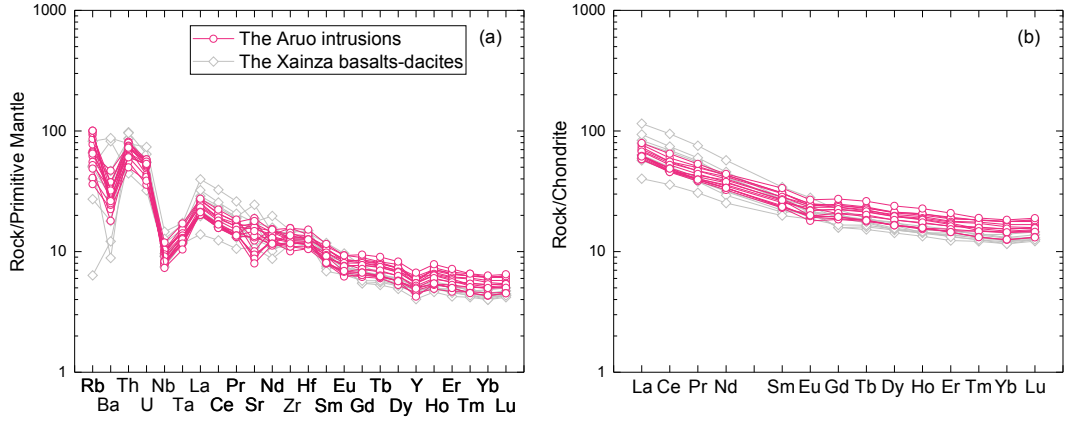


**FIGURE 8.** (**a**) Primitive mantle-normalized trace element patterns and (**b**) chondrite-normalized rare earth element data for the Aruo intrusions. Normalizing values are from Sun and McDonough (1989). The data of the Xainza basalts-dacites are from Kang (2009).

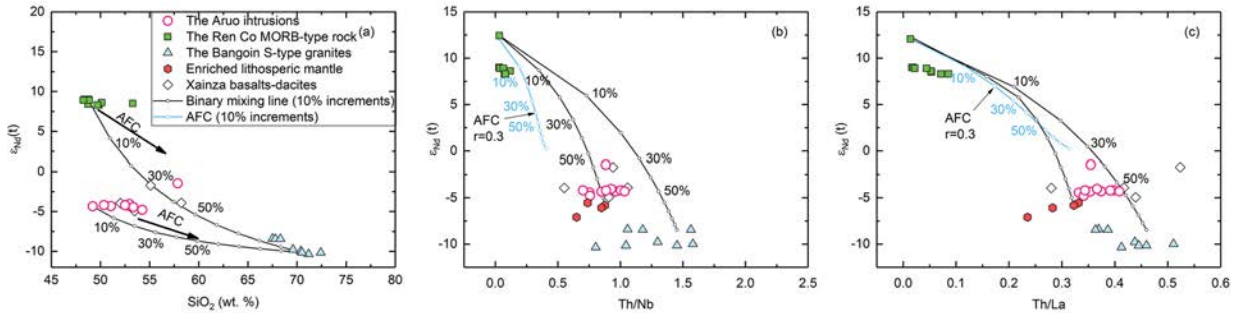


**Figure 9.** Plots of (**a**) whole-rock $SiO_2$ vs. $\varepsilon_{Nd}(t)$, (**b**) Th/Nb vs. $\varepsilon_{Nd}(t)$, and (**c**) Th/La vs. $\varepsilon_{Nd}(t)$ for the Aruo intrusions. The AFC simulation was performed using the method described by Ersoy and Helvacı (2010); "r" refers to the assimilation rate in AFC models. In **b**, the assimilated end-member is represented by one sample of the Baingoin S-type granites (16BG49-2; Hu et al. 2019), and the deleted end-member is the Jurassic Ren Co MORB-type rock (sample 15T269; Tang et al. 2020). The data of lithospheric mantle-derived gabbros are from Zhu et al. (2012) and Hu et al. (2018), and of the Xainza basalts-dacites are from Kang (2009).

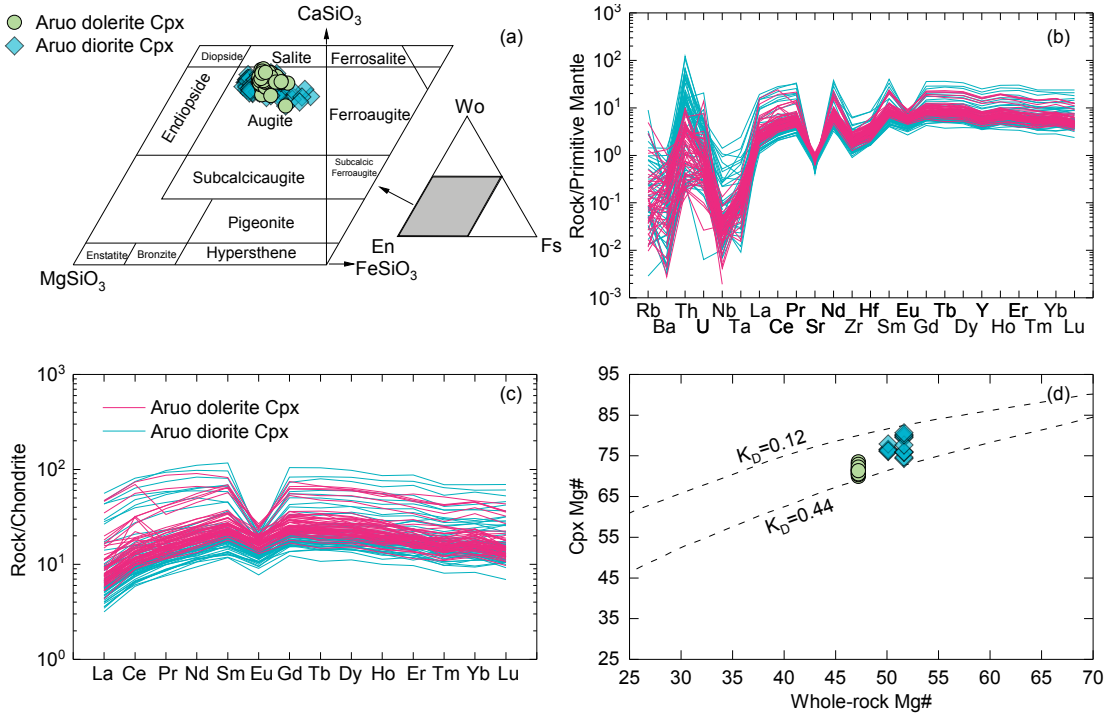


**Figure 10.** (**a**) $CaSiO_3$-$MgSiO_3$-$FeSiO_3$ diagram showing the compositions of pyroxene (Morimoto et al. 1988), (**b**–**c**) primitive mantle normalized multi-element patterns and chondrite-normalized REE patterns for clinopyroxenes of the Aruo dolerites and diorites, (**d**) plot of clinopyroxene Mg# vs. whole-rock Mg# values, showing the melt-clinopyroxene equilibrium band.

(0.58–0.78 wt%; Online Materials[1] Table S8).

The trace element composition of clinopyroxenes in dolerite and diorite are similar in general. The chondrite-normalized REE pattern is characterized by depletion in LREE relative to HREE [$(La/Sm)_N$ = 0.23–0.86; $(La/Yb)_N$ = 0.33–1.21, where the average is average 0.51]. The primitive mantle-normalized trace element patterns show Nb, Ta, Zr, Hf, Sr, and Eu depletion relative to the neighboring elements and variable Ba, Th, and U enrichments (Fig. 10). The Sr values are uniform or slightly decreasing with decreasing Mg#, which, together with the negligible positive Eu anomalies and the petrographic observations, implies that clinopyroxene crystallized simultaneous with and/or after plagioclase (Fig. 11).

The initial Pb isotopes of clinopyroxene are corrected to 120 Ma following the methods of Zhang et al. (2014). Clinopyroxene from two dolerite samples (19AR-04 and 19AR-05) exhibit relatively homogeneous Pb isotopic compositions with $(^{208}Pb/^{206}Pb)_i$ and $(^{207}Pb/^{206}Pb)_i$ ratios varying from 2.102 to 2.145 and from 0.844 to 0.863, respectively (Figs. 11c–11d; Online Materials[1] Table S9).

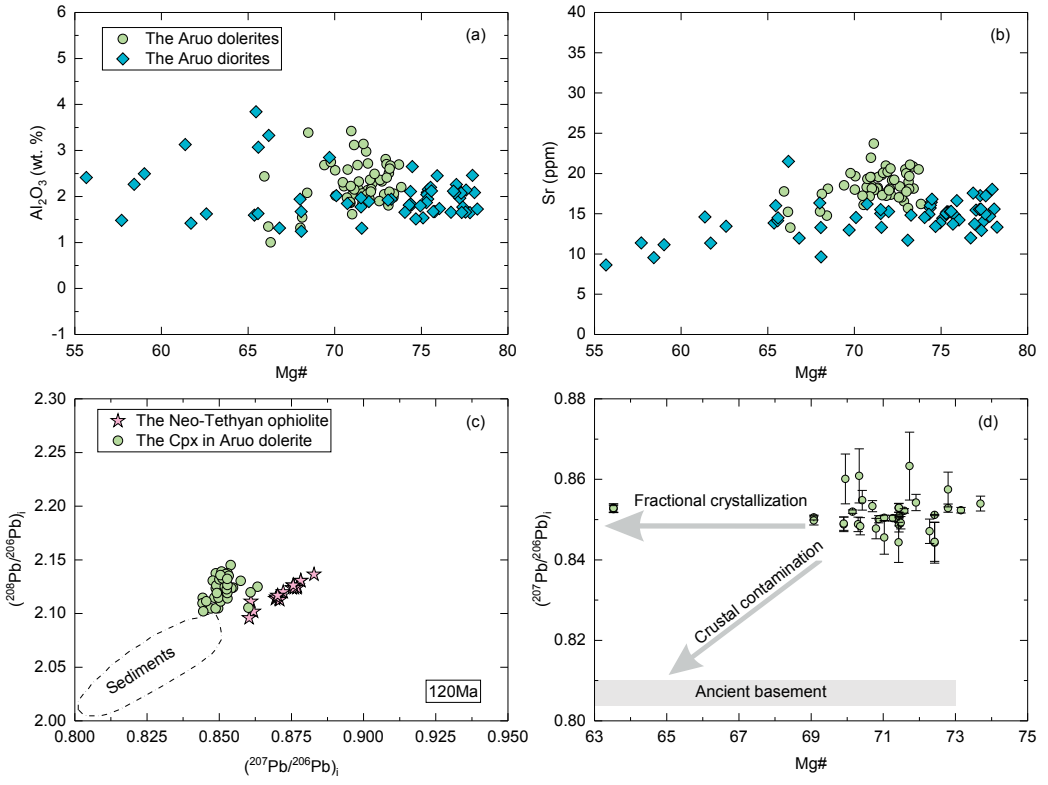


**Figure 11.** Plots of (**a**) $Al_2O_3$ vs. Mg# values, (**b**) Sr vs. Mg# values, (**c**) $(^{208}Pb/^{206}Pb)_i$ vs. $(^{207}Pb/^{206}Pb)_i$, and (**d**) $(^{207}Pb/^{206}Pb)_i$ vs. Mg# values for clinopyroxene from the Aruo intrusions. The data of Neo-Tethyan ophiolite are from Xu and Castillo (2004) and Zhang et al. (2005), and of the ancient basement are inferred from Huang et al. (2017). The field of sediment is from Qian et al. (2017).

## Discussion

### Physical condition during crystallization

The chemistry of clinopyroxene is sensitive to melt temperature and pressure, but most thermometers and barometers require an initial assumption of pressure and temperature, respectively. The clinopyroxene-melt thermobarometer of Putirka et al. (2003) can simultaneously estimate the crystalliza-tion pressure and temperature if the equilibrated liquid (e.g., whole-rock, glass, or matrix) composition is known. However, the premise of using this thermobarometer is that the clinopyroxene should be chemically in equilibrium with the melt (usually represented by the glass, matrix, or whole-rock composition). The equilibrium can be tested by the Fe-Mg exchange coefficient $[K_D(Fe\text{-}Mg)^{clinopyroxene–melt}]$ between the clinopyroxene and the assumed melt, which should be 0.28 ± 0.16 (±2σ; Putirka 2008) if they are chemically equilibrated. As shown in Figure 10d, the clinopyroxene and whole-rock compositions are equilibrated, providing us access to adequately use the clinopyroxene-melt thermobarometer. The clinopyroxenes of dolerite crystallized under temperatures of 1149 to 1197 °C (average temperature is 1162 °C) and pressures of 590 to 935 MPa (corresponding to a continental depth of 18 to 29 km). The clinopyroxenes of diorite crystallized at lower temperatures of 999–1094 °C (average temperature is 1050 °C) and pressures of 49–515 MPa (corresponding to a continental depth of 2 to 17 km; Online Materials[1] Table S7).

Amphibole compositions provide us with another independent access to infer the physicochemical conditions of melt crystallization. By using the methods of Ridolfi et al. (2010), the temperatures, $H_2O$ contents, and pressures for magma in equilibrium with amphibole grains in the Aruo intrusions, are 863–937 °C, 4.2–5.9 wt%, and 190–280 MPa (corresponding to a continental depth of 9 to 13 km), respectively (Online Materials[1] Table S8). Because the Aruo intrusions are not cumulate rocks, the physicochemical estimations based on the mineral geothermobarometer are indicative of the pressure, temperature, and water content occurring in the magma during the crystallization of the target minerals. Thus, these results suggest that the parental magmas of the Aruo intrusions were $H_2O$-rich and underwent a polybaric evolution with the crystallization of clinopyroxene at depth (18–29 km) and that of amphibole at shallower levels (9–13 km).

### Nature of the source

Magma differentiation. The MgO (3.7–5.9 wt%), Mg# (42.1–47.2), Cr (8.22–71.0 ppm), and Ni (2.26–12.5 ppm) values of the Aruo intrusions are much lower than those of primary mantle-derived melts (Mg# = 68–76, Cr >300 ppm, Ni >200 ppm; Roeder and Emslie 1970), indicating a considerable degree of differentiation of their parent magma. Fractional crystallization and assimilation of pre-existing continental crust are two end-member mechanisms responsible for the observed chemical variations in the Aruo intrusions. The heterogeneous zircon Hf isotopes plausibly suggest that intracrustal assimilation or mixing might have

played an important role during magmatic evolution. However, as demonstrated by MELTS simulation and simple binary mixing modeling of magma evolution, crustal assimilation fails to explain the initial increase in $Al_2O_3$ concentrations followed by the $Al_2O_3$ decrease and $SiO_{2\ increase}$ (Fig. 7b). Moreover, a significant crustal assimilation is inconsistent with the variations in Th/Nb, Th/La, and Nd isotopes (Fig. 9). Therefore, we suggest that the chemical diversity of the Aruo intrusions are mainly controlled by crystallization differentiation, and we will test the reason(s) of the zircon Hf isotope heterogeneity in detail later. Simulation results and the negative correlations of $SiO_2$ with MgO, $Fe_2O_3^T$, $TiO_2$, and CaO (Fig. 7) indicate that olivine, clinopyroxene, and Fe-Ti oxides were the main fractionated phases (Fig. 2). The negligible to slightly positive Eu anomalies (δEu = 0.87–1.02; Fig. 8; Online Materials[1] Table S5), and the increasing in $Al_2O_3$ contents with increasing $SiO_2$ contents until 60 wt% (Fig. 7b) suggest minimal or no fractionation of plagioclases in the mafic to intermediate rocks.

Origin of the zircon Hf isotope heterogeneity. There are several alternative ways to account for the zircon Hf isotope heterogeneity of the Aruo rocks. First, we need to exclude that the Hf variability is related to analytical issues. An inaccurate interference correction can lead to a miscalculation of $^{176}Hf/^{177}Hf$ values, and analytical inaccuracies are amplified proportionally to the $^{176}Yb/^{177}Hf$ of the analyzed crystals. For example, a 0.1% inaccurate correction will lead to a miscalculation of $^{176}Hf/^{177}Hf$ values by about ~2 $\varepsilon_{Hf}$ units for zircon crystals with $^{176}Yb/^{177}Hf$ as low as 0.05 (Fisher et al. 2014; Farina et al. 2014). Moreover, an inaccurate interference correction should give rise to a positive correlation between $^{176}Yb/^{177}Hf$ and $^{176}Hf/^{177}Hf$ (Fisher et al. 2014). The great majority of zircons in the Aruo rocks have $^{176}Yb/^{177}Hf$ ranging between 0.02 and 0.05, together with no positive correlation between $^{176}Hf/^{177}Hf$ and $^{176}Yb/^{177}Hf$ (Online Materials[1] Fig. S2a), suggesting the Hf isotopic variability described reflects a natural process rather being an analytical artifact.

The $\varepsilon_{Hf}(t)$ variability in zircon thus argues for the involvement of isotopically different components. The Lhasa lithospheric mantle has suffered multiple stages of metasomatism via oceanic or continental subduction since the Proterozoic (e.g., Yin and Harrison 2000; Zhu et al. 2011a; Hu et al. 2018; etc.), which should have extremely enriched the Hf isotopic signature (Fig. 5a; Zhu et al. 2012; Hu et al. 2018). Besides, the central Lhasa Terrane is underlain by an ancient basement as demonstrated by the local exposure of high-grade metamorphic rocks and the negative zircon $\varepsilon_{Hf}(t)$ values of the Late Triassic-Jurassic granitoids (Zhu et al. 2011b; Fig. 5a). Therefore, the depleted end-member can only be the asthenospheric mantle, which gains support from the fact that the highest $\varepsilon_{Hf}$ values in the Aruo zircons are similar to those observed in the regional Jurassic MORB-type rocks [$\varepsilon_{Hf}(t)$ = +12.8 and +17.7] (Tang et al. 2020).

These two components (enriched and depleted end-members) are both participating in the petrogenesis of the Ario intrusion, and four hypotheses can be formulated to account for the origin of these rocks: (1) the enriched components come from the lithospheric mantle; (2) the enriched component comes from the assimilation of an ancient basement (lower continental crust) with low $\varepsilon_{Hf}(t)$ and $\varepsilon_{Nd}(t)$ but equilibrated with the mantle for oxygen; (3) the addition of an upper crustal component at shallow level via assimilation of the country rocks; and (4) partial melting of the asthenosphere (depleted component) metasomatized by a crustal (sediment) component coming from the oceanic slab. Below we test the four hypotheses in detail.

First, the constant $^{208}Pb/^{206}Pb$ values of the Aruo clinopyroxene are inconsistent with mixing between magmas derived from the asthenospheric and lithospheric mantle. This view is further supported by the binary mixing model of trace element ratios (in particular Th/La; Fig. 9). The basement of the Lhasa Terrane is directly sampled by recently discovered Triassic gneiss exposed in the Rendui area (Fig. 1a; Zhou 2017), yet, the Sr-Nd-Pb isotopic signature of this gneiss remains unknown. The Early Cretaceous Cuoqen metaluminous dacites are interpreted as melts of the Lhasa basement (Huang et al. 2017), as supported by their similar zircon $\varepsilon_{Hf}$ values with the metamorphic zircons of Rendui gneiss that are much higher than the S-type granites in central Lhasa Terrane. It is, therefore, reasonable to use the Sr-Nd-Pb isotopes of the Cuoqen dacites to represent the Lhasa basement. The constant $^{208}Pb/^{206}Pb$ values of clinopyroxene crystallized at 590–935 MPa preclude any significant contamination with the lower continental crust (Fig. 11).

Disentangling mantle source heterogeneity from shallow crustal contamination by using radiogenic isotopes alone is not straightforward. Zircons of the Baingoin S-type granites nearby the study area, which were formed by anatexis of Lhasa sediment-rich upper crustal assemblages, display markedly varied $\varepsilon_{Hf}$ values (–21.36 to –0.02; Hu et al. 2019). Asthenospheric melts assimilating upper crustal rocks will, therefore, crystallize zircons with high-$\varepsilon_{Hf}$ core and low-$\varepsilon_{Hf}$ rim, though the degree of $\varepsilon_{Hf}$ variation depends on the Hf isotopic composition and the amount of sediment assimilated. However, both low- and high-$\varepsilon_{Hf}$ cores are developed in the Aruo zircons, and the Hf isotope composition changes irregularly (Fig. 3). Thus, it is unlikely the Hf variability in zircon of Aruo intrusions resulted from mixing of asthenospheric and crustal component. Additional supports for this view include: (1) ancient xenocrystic zircons are absent in the Aruo intrusions, yet our binary mixing modeling implies assimilation of a considerable amount (30–50%) of upper crustal sediment would be needed to achieve the low-$\varepsilon_{Nd}(t)$ values and Th/Nb and Th/La ratios of the Aruo rocks (Figs. 9c–9d). Such large-scale assimilation would undoubtedly leave petrological traces that are not witnessed in these rocks. (2) The whole-rock $\varepsilon_{Nd}(t)$ values of the Aruo intrusions remain constant or even slightly higher with increasing $SiO_2$ contents, at odds with the trend of assimilation of an ancient crustal component (Fig. 9a). (3) There are no correlations between the Hf isotopes and key trace element concentrations in zircon that are sensitive to physicochemical variations, for example Th/U ratios and Hf contents for the degree of magma differentiation and temperature, Yb/Gd for crystallization depth (Online Materials[1] Fig. S2; e.g., Kemp et al. 2007; Barth et al. 2013; Cooper et al. 2014; Grimes et al. 2015).

The spread of data within Hf-O isotope space provides an independent means of assessing mixtures of crustal and mantle reservoirs (Roberts et al. 2013). The zircon oxygen isotopes are relatively uniform, albeit they are slightly higher than pristine mantle values and thus provide further evidence of incorporation of supra-crustal materials into the petrogenetic process (e.g., Valley et al. 2005). Given that oxygen concentrations in sediments, crust and mantle are broadly similar, the shape of mixing/assimilation curves on a Hf-O plot is largely controlled by the Hf concentrations

of the various components. The lack of covariation between Hf and O isotopes from the same grains by the Aruo zircons (Fig. 5b) suggests the mixed components have contrasting Hf concentrations (i.e., depleted mantle and sediment rather than basaltic melt and sediment). The elevated $\delta^{18}O$ of high-$\varepsilon_{Hf}$ zircon suggests the introduction of a high-$\delta^{18}O$ component relatively early on in magma differentiation (Valley et al. 2005; Kemp et al. 2007), that is, to the mantle source region. The lower $^{207}Pb/^{206}Pb$ and $^{208}Pb/^{206}Pb$ isotopic values of the Aruo clinopyroxenes than that of the Neo-Tethyan ophiolite further support the interpretation that recycled sediment was incorporated into the depleted mantle (Fig. 11c). Besides, the high-whole-rock Th/La ratios (>0.29; Online Materials[1] Table S5) and their negative relationship with the Sm/La ratios (not shown), are consistent with the results of sediment-mantle mixing (Plank 2005). Our modeling shows that partial melting of asthenosphere mantle with the addition of 1–4% terrigenous sediment can explain well the Hf-O isotope variability of the Aruo zircons (Fig. 5b). We note, however, that we must explain why the whole-rock trace element and Nd isotopes distributions, as well as Pb isotopes of clinopyroxene of the Aruo intrusions, are relatively uniform (Figs. 8, 9, and 11). These phenomena argue that the amounts of recycled sediments are probably not the primary control of the Hf isotope variation. The Hf concentrations and isotopes of subducted terrestrial sediments are primarily controlled by zircon (e.g., Carpentier et al. 2009; Nebel et al. 2011), which themselves may be heterogeneous in Hf isotopes as regionally manifested by the Baingoin S-type granites described above (Hu et al. 2019). Zircon, however, contributes little Nd and Pb to the whole rock budget compared to Zr and Hf. Thus, we argue that zircons in subducted sediments were fully dissolved, and the Hf isotopes of the dissolved crystals governed the Hf isotopic signature of the metasomatized mantle with negligible influence on Nd-Pb isotopes and most other trace elements. Although the true composition of subducted sediments in this area is unknown, the Lhasa Terrane suffered several phases of oceanic slab subduction and continental collision prior to and during its assembly with the Gondwana supercontinent. We suggest that this complex history justifies the variability in Hf isotopes of detrital zircon from Paleozoic-Mesozoic sediments (e.g., Zhu et al. 2009). Accordingly, we propose that the Hf isotope heterogeneity in zircon of Aruo intrusions most likely was inherited from a mantle source metasomatically enriched with Hf from sedimentary sources like those from which the Baingoin S-type granites were formed.

## Implications

The results of our study have two main implications: one is related to the regional tectonic evolution, and the other is more general and concerns the use of zircon Hf isotope data to trace magmatic evolution and the growth of continental crust.

### Regional tectonic evolution

Prior to the India-Asia collision, the Andean-type subduction of Neo-Tethyan lithosphere along the southern margin of Lhasa Terrane formed prolonged Mesozoic magmatism with several phases of flare-up (Ji et al. 2009). The underplating of depleted mantle-derived materials during the oceanic slab subduction led to the growth of large amounts of juvenile crust in the southern Lhasa Terrane (e.g., Ma et al. 2013a; Zhu et al. 2017). However, the tectonomagmatic evolution of the central-north Lhasa Terrane remains enigmatic, although widespread Early Cretaceous magmatism with a flare-up at ca. 120–110 Ma has been identified (e.g., Zhang et al. 2012; Li et al. 2018; Zeng et al. 2020). Previous studies focused on intermediate-felsic magmatic rocks with relatively little attention to contemporaneous mantle-derived mafic rocks, given their rare exposure in the central Lhasa Terrane.

Three competing hypotheses have been proposed to explain the Early Cretaceous tectonomagmatic evolution of the central-north Lhasa Terrane: (1) intra-block underthrusting and/or post-collision lithospheric delamination following the collision between Lhasa and Qiangtang terranes (Hu et al. 2017); (2) southward subduction, roll-back and eventually break-off of the Bangong-Nujiang Oceanic lithosphere (Wang et al. 2020); (3) northward subduction and roll-back of the Neo-Tethyan lithosphere (e.g., Zhang et al. 2012; Ma et al. 2013b; Zeng et al. 2020). The low-K tholeiitic to calk-alkaline evolutionary trend (Fig. 6b), the negative Nb-Ta anomalies with enrichment in most LILEs (Fig. 8), and the presence of amphibole crystals and high-melt $H_2O$ contents of the studied Aruo dolerites and diorites are characteristic of arc-type rocks (Zhou et al. 2006), and accordingly are more in support of their formation in a subduction-related, rather than post-collisional setting. Moreover, zircon Hf-O isotopes and whole-rock Th/La ratios and Nd isotopes (Figs. 5 and 9) collectively suggest the recycling of terrigenous sediments into the depleted mantle. The lack of negative Zr-Hf anomalies (Fig. 8), together with the suprachondritic Zr/Hf (34.3–41.2) and Zr/Y (5.0–7.0) ratios of the Aruo intrusions, imply that the zircons in the subducted sediments might have been completely destroyed.

The dissolution of zircon in a sediment-derived melt is governed by zircon saturation (i.e., Zr solubility in the melt, which increases with temperature and possibly decreases with pressure; Watson and Harrison 1983; Rubatto and Hermann 2007). Melting experiments using sedimentary starting materials show that temperatures in excess of 925 °C are needed to fully dissolve zircon (Hermann and Rubatto 2009). This is why mafic arc rocks with high-Zr/Y ratios and positive Zr-Hf anomalies are rare and are mainly found in hot subduction zones (e.g., the high-Zr/Y basalts from the Sumisu Rift; Hirai et al. 2018). For the Aruo intrusions, a special tectonic environment, therefore, is inferred to gain slab surface temperature high enough to dissolve zircon in subducted sediments, regardless of whether the sediment is carried by a Neo-Tethyan slab or Bangong Tethyan slab. Based on a synthesis of independent observations, we (Zeng et al. 2020) have recently proposed a model of steepening and roll-back of flatly northwards subducted Neo-Tethyan oceanic lithosphere at ca. 120–110 Ma to explain the observed late Early Cretaceous tectonic-magmatic complexity (Fig. 13). These observation are (Fig. 12): (1) Jurassic-Early Cretaceous magmatism migrated northward throughout the Lhasa terrane and finally migrated southward at ~110 Ma; (2) rapid cooling of the Xiabie and Baingoin granites started at ~120 Ma, (Kapp et al. 2007; Volkmer et al. 2014); (3) deposition in the Coqen Basin of limestone of the Langshan Formation and limestone to clastic red beds of the Takena Formation took place at ca. 113–96 Ma and ca. 105–90 Ma, respectively (Fig. 12; Sun et al. 2015; Leier et al. 2007); and (4) no southward subduction-related accretionary complex

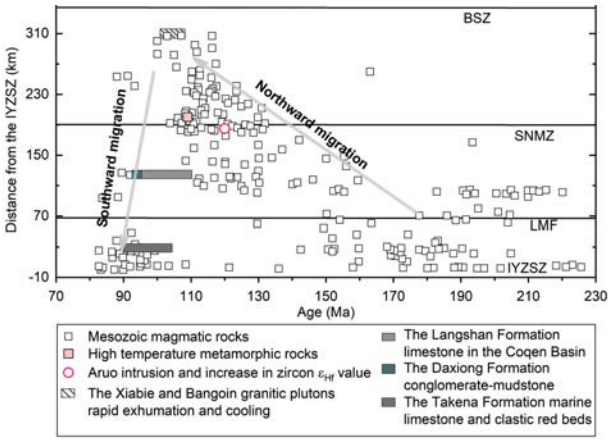


**Figure 12.** Temporal and spatial distribution of Mesozoic magmatic rocks in the Lhasa Terrane (after Zeng et al. 2020 and references therein). The zircon $\varepsilon_{Hf}(t)$ values of magmatic rocks in the central Lhasa Terrane notably increase at ca. 120 Ma. IYZSZ = Indus-Yarlung Zangbo Suture Zone; BSZ = Bangong Suture Zone; SNMZ = ShiquanheNamuTso ophiolite mélange zone; LMF = Lobuodui-Milashan Fault.

is preserved in the northern Lhasa Terrane (Hu et al. 2022). The Aruo intrusions provide new evidence of a change in the tectonic regime of the central-northern Lhasa Terrane at ca. 120 Ma. We propose that the rising asthenosphere in response to the change in the Neo-Tethyan subduction angle could provide the additional heat required to dissolve zircon in the subducted sediments as manifested by the geochemistry of the Aruo intrusions (Fig. 13).

### The use of zircon Hf isotopes to track magmatic evolution and crust growth

Our study reports substantial Hf isotope variation in zircon crystallized from mantle-derived magma that requires a source containing components of depleted asthenosphere and pre-existing mature crust. Our combined clinopyroxene and whole-rock chemical and isotopic investigation limit contamination or mixing of crust-derived melts with mantle-derived melts in the upper crust as the cause of heterogeneous Hf isotopes. Instead, we suggest that the heterogeneity was inherited through metasomatism of depleted asthenospheric mantle by terrestrial sediments. Magmas derived from these sources may pass this Hf isotope heterogeneity on to granitoids either by fractional crystallization or by partially melting, which may be misunderstood as evidence of magma mixing or disequilibrium melting of the crust if only zircon Hf isotopes in granitoids are studied. Therefore, we emphasize the necessity of isotopic investigations on minerals crystallizing before zircons, and combined O isotopic and whole-rock data, to correctly resolve the mechanism of recycling of pre-existing continental crust to the source of arc rocks as shown by complex zircon Hf isotopes.

In addition, our study provides the first evidence to show that the increasing zircon Hf isotope values of Early Cretaceous magmatic rocks at ca. 120 Ma (Fig. 12) was related to the underplating of depleted mantle-derived materials, namely juvenile continental crustal growth. Because of the addition of terrestrial sediments to the wedge mantle, the Hf isotopic model ages (258–1224 Ma) are much older than the formation of this juvenile crust. Importantly, although regional geological and geochemical data do provide testimony of crustal growth (Fig. 5), even some of the zircons in the Aruo dolerites and diorites with MORB-like depleted Hf isotopes will probably be omitted as evidence of continental crustal growth following the landmark criterion ($\delta^{18}O$ +5.9‰ in 2σ level) proposed by Kemp et al. (2007). We, therefore, hold a conservative view on simply using detrital zircon Hf-O isotopes to infer the timing and rate of continental crustal growth through time regionally and globally, which certainly is useful but should be accompanied with other

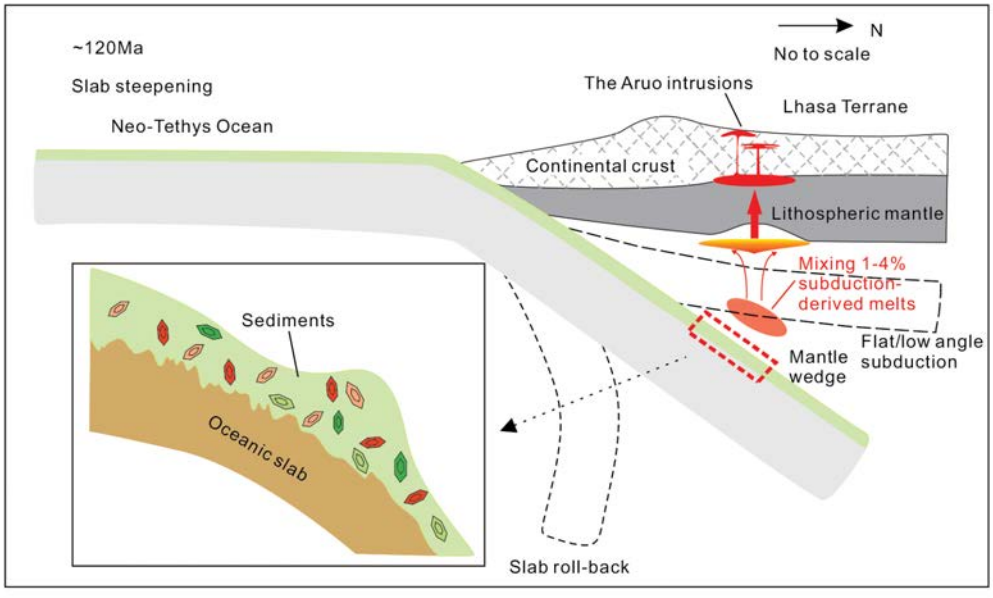


**Figure 13.** Schematic model of the genesis of the Aruo intrusions. The subduction-derived melts incorporate Hf derived from heterogeneous detrital zircon components. Without effectively mixing, these components crystallize magmatic zircon that captures this sedimentary heterogeneity.

additional constraints either from zircons themselves (e.g., the Th/Nb ratios as a proxy of melt $SiO_2$ content; Turner et al. 2020) or minerals crystallized before zircons.

## Acknowledgments

We are grateful to Christopher Spencer and an anonymous reviewer for their insightful reviews and to Paul Tomascak for his excellent editorial work, which substantially improved the manuscript. Assistance from Ding-Shuai Xue, Dan-Ping Zhang, Bing-Yu Gao, Wen-Jun Li, Yong-Hai Yuan, Hong-Xia Yu, Zheng-Lin Li, Yin-Hui Zhang, Le Zhang, Pei-Zhi Wang, and Hao-Ran Dou are sincerely acknowledged during the geochemical analyses.

## Funding

This research is supported by: the Natural Science Foundation of China (42121002); the Second Tibetan Plateau Scientific Expedition (STEP) program (2019QZKK0702); the Fundamental Research Funds for the Central Universities (376202107 and 292019063); the National Key and Development Project of China (2020YFA0714800); the Natural Science Foundation of China (92055208, 42273045, and 41903034), and the 111Project of the China Ministry of Science and Technology (BP0719021). Ming-Jian Li is supported by a scholarship from the China Scholarship Council (202106400045).

## References cited

Bao, Z.A., Zong, C.L., Fang, L.R., Yuan, H.L., Chen, K.Y., and Dai, M.N. (2018) Determination of Hf-Sr-Nd isotopic ratios by MC-ICP-MS using rapid acid digestion after flux-free fusion in geological materials. Acta Geochimica, 37, 244–256, https://doi.org/10.1007/s11631-017-0207-x.

Barth, A.P., Wooden, J.L., Jacobson, C.E., and Economos, R.C. (2013) Detrital zircon as a proxy for tracking the magmatic arc system: The California arc example. Geology, 41, 223–226, https://doi.org/10.1130/G33619.1.

Carpentier, M., Chauvel, C., Maury, R.C., and Mattielli, N. (2009) The "zircon effect" as recorded by the chemical and Hf isotopic compositions of Lesser Antilles forearc sediments. Earth and Planetary Science Letters, 287, 86–99, https://doi.org/10.1016/j.epsl.2009.07.043.

Cooper, G.F., Wilson, C.J., Charlier, B.L., Wooden, J.L., and Ireland, T.R. (2014) Temporal evolution and compositional signatures of two supervolcanic systems recorded in zircons from Mangakino volcanic centre, New Zealand. Contributions to Mineralogy and Petrology, 167, 1018, https://doi.org/10.1007/s00410-014-1018-2.

Dilek, Y. and Furnes, H. (2011) Ophiolite genesis and global tectonics: Geochemical and tectonic fingerprinting of ancient oceanic lithosphere. Geological Society of America Bulletin, 123, 387–411, https://doi.org/10.1130/B30446.1.

Elburg, M., Vroon, P., van der Wagt, B., and Tchalikian, A. (2005) Sr and Pb isotopic composition of five USGS glasses (BHVO-2G, BIR-1G, BCR-2G, TB-1G, NKT-1G). Chemical Geology, 223, 196–207, https://doi.org/10.1016/j.chemgeo.2005.07.001.

Elhlou, S., Belousova, E., Griffin, W.L., Pearson, N.J., and O'Reilly, S.Y. (2006) Trace element and isotopic composition of GJ-red zircon standard by laser ablation. Geochimica et Cosmochimica Acta, 70, A158, https://doi.org/10.1016/j.gca.2006.06.1383.

Ersoy, Y. and Helvacı, C. (2010) FC-AFC-FCA and mixing modeler: A Microsoft® Excel© spreadsheet program for modeling geochemical differentiation of magma by crystal fractionation, crustal assimilation and mixing. Computers & Geosciences, 36, 383–390, https://doi.org/10.1016/j.cageo.2009.06.007.

Farina, F., Stevens, G., Gerdes, A., and Frei, D. (2014) Small-scale Hf isotopic variability in the Peninsula pluton (South Africa): The processes that control inheritance of source $^{176}Hf/^{177}Hf$ diversity in S-type granites. Contributions to Mineralogy and Petrology, 168, 1065, https://doi.org/10.1007/s00410-014-1065-8.

Farina, F., Dini, A., Davies, J.H., Ovtcharova, M., Greber, N.D., Bouvier, A.S., Baumgartner, L., Ulianov, A., and Schaltegger, U. (2018) Zircon petrochronology reveals the timescale and mechanism of anatectic magma formation. Earth and Planetary Science Letters, 495, 213–223, https://doi.org/10.1016/j.epsl.2018.05.021.

Finch, M.A., Weinberg, R.F., Barrote, V.R., and Cawood, P.A. (2021) Hf isotopic ratios in zircon reveal processes of anatexis and pluton construction. Earth and Planetary Science Letters, 576, 117215, https://doi.org/10.1016/j.epsl.2021.117215.

Fisher, C.M., Vervoort, J.D., and Hanchar, J.M. (2014) Guidelines for reporting zircon Hf isotopic data by LA-MC-ICPMS and potential pitfalls in the interpretation of these data. Chemical Geology, 363, 125–133, https://doi.org/10.1016/j.chemgeo.2013.10.019.

Gasparon, M., Hilton, D.R., and Varne, R. (1994) Crustal contamination processes traced by helium isotopes: Examples from the Sunda arc, Indonesia. Earth and Planetary Science Letters, 126, 15–22, https://doi.org/10.1016/0012-821X(94)90239-9.

Ghiorso, M.S. and Sack, R.O. (1995) Chemical mass transfer in magmatic processes IV. A revised and internally consistent thermodynamic model for the interpolation and extrapolation of liquid-solid equilibria in magmatic systems at elevated temperatures and pressures. Contributions to Mineralogy and Petrology, 119, 197–212, https://doi.org/10.1007/BF00307281.

Griffin, W.L., Pearson, N.J., Belousova, E., Jackson, S.V., Van Achterbergh, E., O'Reilly, S.Y., and Shee, S.R. (2000) The Hf isotope composition of cratonic mantle: LAM-MC-ICPMS analysis of zircon megacrysts in kimberlites. Geochimica et Cosmochimica Acta, 64, 133–147, https://doi.org/10.1016/S0016-7037(99)00343-9.

Grimes, C.B., Wooden, J.L., Cheadle, M.J., and John, B.E. (2015) "Fingerprinting" tectono-magmatic provenance using trace elements in igneous zircon. Contributions to Mineralogy and Petrology, 170, 46, https://doi.org/10.1007/s00410-015-1199-3.

Hastie, A.R., Kerr, A.C., Pearce, J.A., and Mitchell, S.F. (2007) Classification of altered volcanic island arc rocks using immobile trace elements: Development of the Th-Co discrimination diagram. Journal of Petrology, 48, 2341–2357, https://doi.org/10.1093/petrology/egm062.

Hawkesworth, C.J. and Vollmer, R. (1979) Crustal contamination versus enriched mantle: $^{143}Nd/^{144}Nd$ and $^{87}Sr/^{86}Sr$ evidence from the Italian volcanics. Contributions to Mineralogy and Petrology, 69, 151–165, https://doi.org/10.1007/BF00371858.

Hermann, J. and Rubatto, D. (2009) Accessory phase control on the trace element signature of sediment melts in subduction zones. Chemical Geology, 265, 512–526, https://doi.org/10.1016/j.chemgeo.2009.05.018.

Hirai, Y., Yoshida, T., Okamura, S., Tamura, Y., Sakamoto, I., and Shinjo, R. (2018) Breakdown of residual zircon in the Izu arc subducting slab during backarc rifting. Geology, 46, 371–374, https://doi.org/10.1130/G39856.1.

Horstwood, M.S., Košler, J., Gehrels, G., Jackson, S.E., McLean, N.M., Paton, C., Pearson, N.J., Sircombe, K., Sylvester, P., Vermeesch, P., and others. (2016) Community-derived standards for LA-ICP-MS U-(Th-) Pb geochronology–Uncertainty propagation, age interpretation and data reporting. Geostandards and Geoanalytical Research, 40, 311–332, https://doi.org/10.1111/j.1751-908X.2016.00379.x.

Hou, Z.Q., Duan, L.F., Lu, Y.J., Zheng, Y.C., Zhu, D.C., Yang, Z.M., Yang, Z.S., Wang, B.D., Pei, Y.R., Zhao, Z.D., and others. (2015) Lithospheric architecture of the Lhasa terrane and its control on ore deposits in the Himalayan-Tibetan orogen. Economic Geology and the Bulletin of the Society of Economic Geologists, 110, 1541–1575, https://doi.org/10.2113/econgeo.110.6.1541.

Hu, P.Y., Zhai, Q.G., Jahn, B.M., Wang, J., Li, C., Chung, S.L., Lee, H.Y., and Tang, S.H. (2017) Late Early Cretaceous magmatic rocks (118–113 Ma) in the middle segment of the Bangong-Nujiang suture zone, Tibetan Plateau: Evidence of lithospheric delamination. Gondwana Research, 44, 116–138, https://doi.org/10.1016/j.gr.2016.12.005.

Hu, P.Y., Zhai, Q.G., Wang, J., Tang, Y., Wang, H.T., and Hou, K.J. (2018) Ediacaran magmatism in the North Lhasa terrane, Tibet and its tectonic implications. Precambrian Research, 307, 137–154, https://doi.org/10.1016/j.precamres.2018.01.012.

Hu, W.L., Wang, Q., Yang, J.H., Zhang, C., Tang, G.J., Ma, L., Qi, Y., Yang, Z.Y., and Sun, P. (2019) Late early Cretaceous peraluminous biotite granites along the Bangong-Nujiang suture zone, Central Tibet: Products derived by partial melting of metasedimentary rocks? Lithos, 344–345, 147–158, https://doi.org/10.1016/j.lithos.2019.06.005.

Hu, X.M., Ma, A.L., Xue, W.W., Garzanti, E., Cao, Y., Li, S.M., Sun, G.Y., and Lai, W. (2022) Exploring a lost ocean in the Tibetan Plateau: Birth, growth, and demise of the Bangong-Nujiang Ocean. Earth-Science Reviews, 229, 104031, https://doi.org/10.1016/j.earscirev.2022.104031.

Huang, Y., Zhao, Z., Zhu, D.C., Liu, Y., Liu, D., Zhou, Q., and Gao, S. (2017) The geochronologic and geochemical constraints on the Early Cretaceous subduction magmatism in the central Lhasa subterrane, Tibet. Geological Journal, 52, 463–475, https://doi.org/10.1002/gj.3112.

Ickert, R.B., Hiess, J., Williams, I.S., Holden, P., Ireland, T.R., Lanc, P., Schram, N., Foster, J.J., and Clement, S.W. (2008) Determining high precision, in situ, oxygen isotope ratios with a SHRIMP II: Analyses of MPI-DING silicate-glass reference materials and zircon from contrasting granites. Chemical Geology, 257, 114–128, https://doi.org/10.1016/j.chemgeo.2008.08.024.

Jackson, S.E., Pearson, N.J., Griffin, W.L., and Belousova, E.A. (2004) The application of laser ablation-inductively coupled plasma-mass spectrometry to in situ U-Pb zircon geochronology. Chemical Geology, 211, 47–69, https://doi.org/10.1016/j.chemgeo.2004.06.017.

Ji, W.Q., Wu, F.Y., Chung, S.L., Li, J.X., and Liu, C.Z. (2009) Zircon U-Pb geochronology and Hf isotopic constraints on petrogenesis of the Gangdese batholith, southern Tibet. Chemical Geology, 262, 229–245, https://doi.org/10.1016/j.chemgeo.2009.01.020.

Kang, Z.Q. (2009) Geochemistry, origin and tectonic implication of the Mesozoic volcanic rocks in Lhasa block. Dissertation, Graduate School of the Chinese Academy of Sciences.

Kang, Z.Q., Xu, J.F., Wilde, S.A., Feng, Z.H., Chen, J.L., Wang, B.D., Fu, W.C., and Pan, H.B. (2014) Geochronology and geochemistry of the Sangri Group Volcanic Rocks, Southern Lhasa Terrane: Implications for the early subduction history of the Neo-Tethys and Gangdese Magmatic Arc. Lithos, 200–201, 157–168, https://doi.org/10.1016/j.lithos.2014.04.019.

Kapp, P. and DeCelles, P.G. (2019) Mesozoic-Cenozoic geological evolution of the Himalayan-Tibetan orogen and working tectonic hypotheses. American Journal of Science, 319, 159–254, https://doi.org/10.2475/03.2019.01.

Kapp, P., DeCelles, P.G., Gehrels, G.E., Heizler, M., and Ding, L. (2007) Geological records of the Lhasa-Qiangtang and Indo-Asian collisions in the Nima area of central Tibet. Geological Society of America Bulletin, 119, 917–933, https://doi.org/10.1130/B26033.1.

Kemp, A.I.S., Hawkesworth, C.J., Foster, G.L., Paterson, B.A., Woodhead, J.D., Hergt, J.M., Gray, C.M., and Whitehouse, M.J. (2007) Magmatic and crustal differentia-

tion history of granitic rocks from Hf-O isotopes in zircon. Science, 315, 980–983, https://doi.org/10.1126/science.1136154.
Kurtz, A.C., Derry, L.A., Chadwick, O.A., and Alfano, M.J. (2000) Refractory element mobility in volcanic soils. Geology, 28, 683–686, https://doi.org/10.1130/0091-7613(2000)28<683:REMIVS>2.0.CO;2.
Leier, A.L., DeCelles, P.G., Kapp, P., and Ding, L. (2007) The Takena Formation of the Lhasa terrane, southern Tibet: The record of a Late Cretaceous retroarc foreland basin. Geological Society of America Bulletin, 119, 31–48, https://doi.org/10.1130/B25974.1.
Li, X.H., Long, W.G., Li, Q.L., Liu, Y., Zheng, Y.F., Yang, Y.H., Chamberlain, K., Wan, D.F., Guo, C.H., Wang, X.-C., and others. (2010) Penglai zircon megacrysts: A potential new working reference material for microbeam determination of Hf-O isotopes and U-Pb age. Geostandards and Geoanalytical Research, 34, 117–134, https://doi.org/10.1111/j.1751-908X.2010.00036.x.
Li, X.H., Tang, G.Q., Gong, B., Yang, Y.H., Hou, K.J., Hu, Z.C., Li, Q.L., Liu, Y., and Li, W.X. (2013) Qinghu zircon: A working reference for microbeam analysis of U-Pb age and Hf and O isotopes. Chinese Science Bulletin, 58, 4647–4654, https://doi.org/10.1007/s11434-013-5932-x.
Li, S.M., Zhu, D.C., Wang, Q., Zhao, Z.D., Sui, Q.L., Liu, S.A., Liu, D., and Mo, X.X. (2014) Northward subduction of Bangong-Nujiang Tethys: Insight from Late Jurassic intrusive rocks from Bangong Tso in western Tibet. Lithos, 205, 284–297, https://doi.org/10.1016/j.lithos.2014.07.010.
Li, S.M., Wang, Q., Zhu, D.C., Stern, R.J., Cawood, P.A., Sui, Q.L., and Zhao, Z. (2018) One or two Early Cretaceous arc systems in the Lhasa Terrane, southern Tibet. Journal of Geophysical Research: Solid Earth, 123, 3391–3413, https://doi.org/10.1002/2018JB015582.
Li, M.J., Zeng, Y.C., Xu, J.F., Huang, F., and Chen, Q. (2020) Petrogenesis of Early Jurassic (ca. 181 Ma) dacitic-rhyolitic volcanic rocks in the Amdo ophiolite mélange, central Tibetan Plateau: Low-pressure partial melts of Bangong-Nujiang Tethys oceanic crust? Geological Journal, 55, 3283–3296, https://doi.org/10.1002/gj.3600.
Liu, Y.S., Hu, Z.C., Gao, S., Günther, D., Xu, J., Gao, C.G., and Chen, H.L. (2008) In situ analysis of major and trace elements of anhydrous minerals by LA-ICP-MS without applying an internal standard. Chemical Geology, 257, 34–43, https://doi.org/10.1016/j.chemgeo.2008.08.004.
Ma, L., Wang, Q., Wyman, D.A., Jiang, Z.Q., Yang, J.H., Li, Q.L., Gou, G.N., and Guo, H.F. (2013a) Late Cretaceous crustal growth in the Gangdese area, southern Tibet: Petrological and Sr-Nd-Hf-O isotopic evidence from Zhengga diorite-gabbro. Chemical Geology, 349–350, 54–70, https://doi.org/10.1016/j.chemgeo.2013.04.005.
Ma, L., Wang, Q., Li, Z.X., Wyman, D.A., Jiang, Z.Q., Yang, J.H., Gou, G.N., and Guo, H.F. (2013b) Early Late Cretaceous (ca. 93 Ma) norites and hornblendites in the Milin area, eastern Gangdese: Lithosphere-asthenosphere interaction during slab roll-back and an insight into early Late Cretaceous (ca. 100–80 Ma) magmatic "flare-up" in southern Lhasa (Tibet). Lithos, 172–173, 17–30, https://doi.org/10.1016/j.lithos.2013.03.007.
Middlemost, E.A. (1994) Naming materials in the magma/igneous rock system. Earth-Science Reviews, 37, 215–224, https://doi.org/10.1016/0012-8252(94)90029-9.
Miyashiro, A. (1975) Volcanic rock series and tectonic setting. Annual Review of Earth and Planetary Sciences, 3, 251–269, https://doi.org/10.1146/annurev.ea.03.050175.001343.
Morimoto, N., Fabries, J., Ferguson, A.K., Ginzburg, I.V., Ross, M., Seifert, F.A., Zussman, J., Aoki, K., and Gottardi, G. (1988) Nomenclature of pyroxenes. American Mineralogist, 73, 1123–1133.
Nebel, O., Vroon, P.Z., van Westrenen, W., Iizuka, T., and Davies, G.R. (2011) The effect of sediment recycling in subduction zones on the Hf isotope character of new arc crust, Banda arc, Indonesia. Earth and Planetary Science Letters, 303, 240–250, https://doi.org/10.1016/j.epsl.2010.12.053.
Pearce, J.A. (2014) Immobile element fingerprinting of ophiolites. Elements, 10, 101–108, https://doi.org/10.2113/gselements.10.2.101.
Plank, T. (2005) Constraints from thorium/lanthanum on sediment recycling at subduction zones and the evolution of the continents. Journal of Petrology, 46, 921–944, https://doi.org/10.1093/petrology/egi005.
Putirka, K.D. (2008) Thermometers and barometers for volcanic systems. Reviews in Mineralogy and Geochemistry, 69, 61–120, https://doi.org/10.2138/rmg.2008.69.3.
Putirka, K.D., Mikaelian, H., Ryerson, F., and Shaw, H. (2003) New clinopyroxene-liquid thermobarometers for mafic, evolved, and volatile-bearing lava compositions, with applications to lavas from Tibet and the Snake River Plain, Idaho. American Mineralogist, 88, 1542–1554, https://doi.org/10.2138/am-2003-1017.
Qian, S.P., Ren, Z.Y., Richard, W., Zhang, L., Zhang, Y.H., Hong, L.B., Ding, X.L., and Wu, Y.D. (2017) Petrogenesis of Early Cretaceous basaltic lavas from the North China Craton: Implications for cratonic destruction. Journal of Geophysical Research: Solid Earth, 122, 1900–1918, https://doi.org/10.1002/2016JB013548.
Ridolfi, F., Renzulli, A., and Puerini, M. (2010) Stability and chemical equilibrium of amphibole in calc-alkaline magmas: An overview, new thermobarometric formulations and application to subduction-related volcanoes. Contributions to Mineralogy and Petrology, 160, 45–66, https://doi.org/10.1007/s00410-009-0465-7.
Roberts, N.M., Slagstad, T., Parrish, R.R., Norry, M.J., Marker, M., and Horstwood, M.S. (2013) Sedimentary recycling in arc magmas: Geochemical and U-Pb-Hf-O constraints on the Mesoproterozoic Suldal Arc, SW Norway. Contributions to Mineralogy and Petrology, 165, 507–523, https://doi.org/10.1007/s00410-012-0820-y.
Roeder, P.L. and Emslie, R. (1970) Olivine-liquid equilibrium. Contributions to Mineralogy and Petrology, 29, 275–289, https://doi.org/10.1007/BF00371276.
Rubatto, D. and Hermann, J. (2007) Experimental zircon/melt and zircon/garnet trace element partitioning and implications for the geochronology of crustal rocks. Chemical Geology, 241, 38–61, https://doi.org/10.1016/j.chemgeo.2007.01.027.
Sláma, J., Košler, J., Condon, D.J., Crowley, J.L., Gerdes, A., Hanchar, J.M., Horstwood, M.S.A., Morris, G.A., Nasdala, L., Norberg, N., and others. (2008) Plešovice zircon—A new natural reference material for U-Pb and Hf isotopic microanalysis. Chemical Geology, 249, 1–35, https://doi.org/10.1016/j.chemgeo.2007.11.005.
Spencer, C.J., Cavosie, A.J., Raub, T.D., Rollinson, H., Jeon, H., Searle, M.P., Miller, J.A., McDonald, B.J., and Evans, N.J. (2017) Evidence for melting mud in Earth's mantle from extreme oxygen isotope signatures in zircon. Geology, 45, 975–978, https://doi.org/10.1130/G39402.1.
Spencer, C.J., Kirkland, C.L., Roberts, N.M.W., Evans, N.J., and Liebmann, J. (2020) Strategies towards robust interpretations of in situ zircon Lu-Hf isotope analyses. Geoscience Frontiers, 11, 843–853, https://doi.org/10.1016/j.gsf.2019.09.004.
Sun, S.S. and McDonough, W.F. (1989) Chemical and isotopic systematics of oceanic basalts: Implications for mantle composition and processes. Special Publication, Geological Society of London, 42, 313–345, https://doi.org/10.1144/GSL.SP.1989.042.01.19.
Sun, G.Y., Hu, X., Sinclair, H.D., BouDagher-Fadel, M.K., and Wang, J. (2015) Late Cretaceous evolution of the Coqen Basin (Lhasa terrane) and implications for early topographic growth on the Tibetan Plateau. Geological Society of America Bulletin, 127, 1001–1020, https://doi.org/10.1130/B31137.1.
Tang, M., Wang, X.L., Shu, X.J., Wang, D., Yang, T., and Gopon, P. (2014) Hafnium isotopic heterogeneity in zircons from granitic rocks: Geochemical evaluation and modeling of "zircon effect" in crustal anatexis. Earth and Planetary Science Letters, 389, 188–199, https://doi.org/10.1016/j.epsl.2013.12.036.
Tang, Y., Zhai, Q.G., Chung, S.L., Hu, P.Y., Wang, J., Xiao, X.C., Song, B., Wang, H.T., and Lee, H.Y. (2020) First mid-ocean ridge-type ophiolite from the Meso-Tethys suture zone in the north-central Tibetan plateau. Geological Society of America Bulletin, 132, 2202–2220, https://doi.org/10.1130/B35500.1.
Turner, S., Wilde, S., Wörner, G., Schaefer, B., and Lai, Y.J. (2020) An andesitic source for Jack Hills zircon supports onset of plate tectonics in the Hadean. Nature Communications, 11, 1241, https://doi.org/10.1038/s41467-020-14857-1.
Valley, J.W. (2003) Oxygen isotopes in zircon. Reviews in Mineralogy and Geochemistry, 53, 343–385, https://doi.org/10.2113/0530343.
Valley, J.W., Lackey, J.S., Cavosie, A.J., Clechenko, C.C., Spicuzza, M.J., Basei, M.A.S., Bindeman, I.N., Ferreira, V.P., Sial, A.N., King, E.M., and others. (2005) 4.4 billion years of crustal maturation: Oxygen isotope ratios of magmatic zircon. Contributions to Mineralogy and Petrology, 150, 561–580, https://doi.org/10.1007/s00410-005-0025-8.
Villaros, A., Buick, I.S., and Stevens, G. (2012) Isotopic variations in S-type granites: An inheritance from a heterogeneous source? Contributions to Mineralogy and Petrology, 163, 243–257, https://doi.org/10.1007/s00410-011-0673-9.
Volkmer, J.E., Kapp, P., Horton, B.K., Gehrels, G.E., Minervini, J.M., and Ding, L. (2014) Northern Lhasa thrust belt of central Tibet: Evidence of Cretaceous–early Cenozoic shortening within a passive roof thrust system. Geological Society of America Special Papers, 507, 59–70, https://doi.org/10.1130/2014.2507(03).
Wang, J.P., Yang, C.H., Lu, S.W., and others. (2002) 1:250,000 Regional Geological Survey Report of the People's Republic of China (Nyima Sheet). Mapping Center Henan Provincial Institute of Geological Survey.
Wang, W., Wang, M., Zhai, Q.G., Xie, C.M., Hu, P.Y., Li, C., Liu, J.H., and Luo, A.B. (2020) Transition from oceanic subduction to continental collision recorded in the Bangong-Nujiang suture zone: Insights from Early Cretaceous magmatic rocks in the north-central Tibet. Gondwana Research, 78, 77–91, https://doi.org/10.1016/j.gr.2019.09.008.
Watson, E.B. and Harrison, T.M. (1983) Zircon saturation revisited: Temperature and composition effects in a variety of crustal magma types. Earth and Planetary Science Letters, 64, 295–304, https://doi.org/10.1016/0012-821X(83)90211-X.
Weis, D., Kieffer, B., Maerschalk, C., Barling, J., de Jong, J., Williams, G.A., Hanano, D., Pretorius, W., Mattielli, N., Scoates, J.S., and others. (2006) High-precision isotopic characterization of USGS reference materials by TIMS and MC-ICP-MS. Geochemistry, Geophysics, Geosystems, 7, Q08006, https://doi.org/10.1029/2006GC001283.
Wu, F.Y., Yang, Y.H., Xie, L.W., Yang, J.H., and Xu, P. (2006) Hf isotopic compositions of the standard zircons and baddeleyites used in U-Pb geochronology. Chemical Geology, 234, 105–126, https://doi.org/10.1016/j.chemgeo.2006.05.003.
Xu, J.F. and Castillo, P.R. (2004) Geochemical and Nd-Pb isotopic characteristics of the Tethyan asthenosphere: Implications for the origin of the Indian Ocean mantle domain. Tectonophysics, 393, 9–27, https://doi.org/10.1016/j.tecto.2004.07.028.
Yin, A. and Harrison, T.M. (2000) Geologic evolution of the Himalayan-Tibetan orogen. Annual Review of Earth and Planetary Sciences, 28, 211–280, https://doi.org/10.1146/annurev.earth.28.1.211.
Zeng, Y.C., Chen, J.L., Xu, J.F., Wang, B.D., and Huang, F. (2016) Sediment melting during subduction initiation: Geochronological and geochemical evidence from the Darutso high-Mg andesites within ophiolite melange, central Tibet. Geochemistry, Geophysics, Geosystems, 17, 4859–4877, https://doi.org/10.1002/2016GC006456.
Zeng, Y.C., Xu, J.F., Chen, J.L., Wang, B.D., Kang, Z.Q., and Huang, F. (2018) Geo-

chronological and geochemical constraints on the origin of the Yunzhug ophiolite in the Shiquanhe-Yunzhug-Namu Tso ophiolite belt, Lhasa Terrane, Tibetan Plateau. Lithos, 300–301, 250–260, https://doi.org/10.1016/j.lithos.2017.11.025.

Zeng, Y.C., Xu, J.F., Huang, F., Li, M.J., and Chen, Q. (2020) Generation of the 105–100 Ma Dagze volcanic rocks in the north Lhasa Terrane by lower crustal melting at different temperature and depth: Implications for tectonic transition. Geological Society of America Bulletin, 132, 1257–1272, https://doi.org/10.1130/B35306.1.

Zeng, Y.C., Xu, J.F., Chen, J.L., Wang, B.D., Huang, F., Xia, X.P., and Li, M.J. (2021a) Early Cretaceous (~138–134 Ma) Forearc Ophiolite and Tectonomagmatic Patterns in Central Tibet: Subduction Termination and Re-initiation of Meso-Tethys Ocean Caused by Collision of an Oceanic Plateau at the Continental Margin? Tectonics, 40, e2020TC006423.

Zeng, Y.C., Xu, J.F., Li, M.J., Chen, J.L., Wang, B.D., Huang, F., and Ren, S.H. (2021b) Late Eocene two-pyroxene trachydacites from the southern Qiangtang Terrane, central Tibetan Plateau: High-temperature melting of overthickened and dehydrated lower crust. Journal of Petrology, 62, egab080, https://doi.org/10.1093/petrology/egab080.

Zhang, S.Q., Mahoney, J.J., Mo, X.X., Ghazi, A.M., Milani, L., Crawford, A.J., Guo, T.Y., and Zhao, Z.D. (2005) Evidence for a widespread Tethyan upper mantle with Indian-Ocean-type isotopic characteristics. Journal of Petrology, 46, 829–858, https://doi.org/10.1093/petrology/egi002.

Zhang, K.J., Zhang, Y.X., Tang, X.C., and Xia, B. (2012) Late Mesozoic tectonic evolution and growth of the Tibetan plateau prior to the Indo-Asian collision. Earth-Science Reviews, 114, 236–249, https://doi.org/10.1016/j.earscirev.2012.06.001.

Zhang, L., Ren, Z.Y., Nichols, A.R., Zhang, Y.H., Zhang, Y., Qian, S.P., and Liu, J.Q. (2014) Lead isotope analysis of melt inclusions by LA-MC-ICP-MS. Journal of Analytical Atomic Spectrometry, 29, 1393–1405, https://doi.org/10.1039/C4JA00088A.

Zhou, X. (2017) Tectonic history and crustal evolution of the northern and central Lhasa Terrane. Dissertation, China University of Geosciences, Mineralogy, Petrology and Economic Geology.

Zhou, M.F., Ma, Y., Yan, D.P., Xia, X., Zhao, J.H., and Sun, M. (2006) The Yanbian terrane (Southern Sichuan Province, SW China): A Neoproterozoic arc assemblage in the western margin of the Yangtze block. Precambrian Research, 144, 19–38, https://doi.org/10.1016/j.precamres.2005.11.002.

Zhu, D.C., Mo, X.X., Niu, Y., Zhao, Z.D., Wang, L.Q., Liu, Y.S., and Wu, F.Y. (2009) Geochemical investigation of Early Cretaceous igneous rocks along an east–west traverse throughout the central Lhasa Terrane, Tibet. Chemical Geology, 268, 298–312, https://doi.org/10.1016/j.chemgeo.2009.09.008.

Zhu, D.C., Zhao, Z.D., Niu, Y., Mo, X.X., Chung, S.L., Hou, Z.Q., Wang, L.Q., and Wu, F.Y. (2011a) The Lhasa Terrane: Record of a microcontinent and its histories of drift and growth. Earth and Planetary Science Letters, 301, 241–255, https://doi.org/10.1016/j.epsl.2010.11.005.

Zhu, D.C., Zhao, Z.D., Niu, Y., Dilek, Y., and Mo, X.X. (2011b) Lhasa terrane in southern Tibet came from Australia. Geology, 39, 727–730, https://doi.org/10.1130/G31895.1.

Zhu, D.C., Zhao, Z.D., Niu, Y., Dilek, Y., Wang, Q., Ji, W.H., Dong, G.C., Sui, Q.L., Liu, Y.S., Yuan, H.L., and others. (2012) Cambrian bimodal volcanism in the Lhasa Terrane, southern Tibet: Record of an early Paleozoic Andean-type magmatic arc in the Australian proto-Tethyan margin. Chemical Geology, 328, 290–308, https://doi.org/10.1016/j.chemgeo.2011.12.024.

Zhu, D.C., Wang, Q., Cawood, P.A., Zhao, Z.D., and Mo, X.X. (2017) Raising the Gangdese mountains in southern Tibet. Journal of Geophysical Research: Solid Earth, 122, 214–223, https://doi.org/10.1002/2016JB013508.

Manuscript received February 28, 2022
Manuscript accepted September 22, 2022
Accepted manuscript online October 6, 2022
Manuscript handled by Paul Tomascak

## Endnote:

[1]Deposit item AM-23-98508. Online Materials are free to all readers. Go online, via the table of contents or article view, and find the tab or link for supplemental materials.